

¹ Modeling ice shelf cavities and calving tabular
² icebergs

A.A. Stern,¹, A. Adcroft¹ and O. Sergienko¹, G. Marquez¹, R. Hallberg¹

³ **Key Points:**

⁴

A. A. Stern, Geophysical Fluid Dynamics Laboratory, Princeton University

A. Adcroft, Geophysical Fluid Dynamics Laboratory, Princeton University

O. Sergienko, Geophysical Fluid Dynamics Laboratory, Princeton University

G. Marquez, Geophysical Fluid Dynamics Laboratory, Princeton University

R. Hallberg, Geophysical Fluid Dynamics Laboratory, Princeton University

5 **Abstract.** The calving of giant icebergs is an important process in the
6 Antarctic freshwater cycle. Iceberg calving can significantly alter the geom-
7 etry of an ice shelf cavity, potentially affecting the circulation within the cav-
8 ity. Furthermore, giant icebergs which break away can drift across large dis-
9 tance, altering ocean circulation, sea ice distributions and bottom water for-
10 mation. However despite its importance, the current generation of nu-
11 merical models is unable to represent this process in a physically realistic way.
12 In this study we develop a model of an ice shelf cavity using a Lagrangian
13 ice shelf. The ice shelf is constructed out of Lagrangian elements which are
14 bonded together by numerical bonds. This Lagrangian framework allows for
15 large pieces of the ice shelf to break away and become tabular icebergs. The
16 model developed in the manuscript is referred to as the Lagrangian Iceberg/Ice
17 Shelf Model (LIISM). This paper provides a description of the LIISM model
18 and discusses a number of the technical elements involved in building a La-
19 grangian ice shelf. To test the model, the LIISM is used to model an ideal-
20 ized ice shelf cavity which was developed as part of the Marine Ice Ocean
21 Modeling Inter-comparison Project (MISOMIP). Results from static ice shelf
22 experiments compare well to results using a more traditional Eulerian ice
23 shelf cavity. The novel capabilities of the LIISM are demonstrated by mod-
24 eling a tabular iceberg breaking away from the idealized ice shelf.

1. Introduction

25 Floating ice shelves cover vast regions of the Antarctic polar oceans. These massive
26 platforms of ice extend deep into the water column, applying large pressures to surface
27 of the ocean, which is often hundreds of meters below global sea level. Beneath the ice
28 shelves, both the bottom topography and the ice shelf geometry play a role in steering
29 ocean currents [Nicholls , 1996; Jenkins et al , 2010; Stern et al , 2014]. The topographic
30 constraint imposed by the ice shelf at the ocean's upper boundary significantly affects the
31 circulation within the ice shelf cavities, and gives the ocean within the ice shelves cavities
32 a unique character.

33 In addition to suppressing the depth of ocean surface, the ice shelves also melt (and
34 break), thus providing a freshwater flux into the ice shelf cavities. Ice shelf melting and
35 breaking are key components in the Antarctic meltwater system, and affect the ocean
36 hydrography and biology both inside and outside of the ice shelf cavities. Some elements
37 of the this Antarctic meltwater system are discussed in the following paragraphs.

38 Within the ice shelf cavities, the input of buoyant meltwater into the ocean creates
39 rising density plumes, which are guided along the ice shelf base, and help drive ocean
40 circulation beneath the ice shelves [MacAyeal , 1984; Holland and Feltham , 2006]. The
41 strength of the circulation within the cavity feeds back onto the ice shelf melt rates, by
42 removing cold water from the cavity, and drawing in warmer waters from the open ocean,
43 thus providing the constant supply of thermal energy needed for continuous ice shelf melt
44 [Lewis and Perkin , 1986; Jacobs et al , 2011].

45 The Antarctic ice shelves are also characterized by large infrequent calving events where
46 massive pieces of the ice shelves break off, to create giant tabular icebergs. Observational
47 estimates suggest that approximately half of Antarctic ice shelf decay is due to iceberg
48 calving, while the other half occurs through ice shelf melting [Depoorter et al , 2013;
49 Rignot et al , 2013]. Calving icebergs' sizes appear to fit a power law distribution, with
50 the majority of icebergs being small ($L < 1$ km), while giant tabular icebergs ($L > 5$ km)
51 account for more than 90% of the icebergs mass [Tournadre et al , 2016]. After calving,
52 icebergs slowly drift away from their mother glaciers, often becoming stuck in sea ice, or
53 become grounded along the Antarctic coast [Lichey and Hellmer , 2001; Dowdeswell and
54 Bamber , 2007]. Giant tabular icebergs also extend deep into the water column, and have
55 to potential to disrupt ocean circulation patterns for months or even years after calving
56 [Robinson et al , 2012; Stern et al , 2015].

57 Melt water from both ice shelf melt and iceberg melt impact the ocean hydrography
58 outside of the ice shelf cavities, influencing sea ice production and bottom water formation
59 [Arrigo et al , 2002; Robinson et al , 2012; Nicholls et al , 2009]. The long distances traveled
60 by giant icebergs before melting means that their meltwater impact is often felt hundreds
61 of kilometers away from their calving origins [Stern et al , 2016]. Melt water injection (and
62 the accompanying upwelling) from ice shelves and icebergs can also influence biological
63 productivity by providing nutrients to the surface ocean or changing sea ice conditions
64 [Arrigo et al , 2002; Vernet et al , 2012; Biddle et al , 2015]. The increased productivity
65 associated with free floating tabular icebergs has been linked with local increases in ocean
66 carbon uptake, potentially large enough to be a significant fraction of the Southern Ocean
67 carbon sequestration [Smith et al , 2007].

68 In recent years society's need for improved projections of future sea level has lead to an
69 increased focus on the Antarctic meltwater system described in the previous paragraphs.
70 This increased interest has led to accelerated efforts to accurately model Antarctic ice shelf
71 cavities [Asay-Davis et al , 2016]. Modeling the ocean beneath the ice shelves presents
72 a unique set of challenges, since (i) the presence of ice shelves provides a rigid upper
73 boundary for the ocean model which is not encountered elsewhere in the ocean, and
74 (ii) melting and breaking ice shelves imply a changing ocean boundary conditions which
75 present numerous numerical difficulties.

76 The earliest models of ocean ice shelf cavities were developed using a static ice shelf
77 with a fixed shape [Hellmer and Olbers , 1989; Determan and Gerdes , 1994; Grosfeld et
78 al , 1997; Holland and Jenkins , 2001; Losch , 2008]. In these models, ice shelf melting
79 was represented through salinity and temperature fluxes, while the ice shelf geometry
80 remained unchanged. Later models of ice shelf cavities allowed the ice shelf geometry
81 to evolve as the ice shelf melted, permitting the study of coupled ocean-ice phenomena
82 [Gladish et al , 2012; Sergienko , 2013]. More recently, dynamic ice shelf models have
83 been coupled the ocean cavity, allowing the study of grounding line migration, which is of
84 key importance for sea level rise projections [Grosfeld and Sandhger , 2004; Goldberg et
85 al , 2012; De Rydt and Gudmundsson , 2016]. As far as we know, all models of ice shelf
86 cavities to date have neglected ice shelf breaking and iceberg detachment.

87 In parallel to these efforts to develop ice shelf cavity models, a number of iceberg drift
88 models have been developed, and have been included in some global General Circulation
89 Models [Bigg et al , 1997; Gladstone et al , 2001; Martin and Adcroft , 2010; Marsh et al ,
90 2015]. These iceberg drift models treat icebergs as Lagrangian point particles, which are

adverted by the flow, and melt according to certain parameterizations for icebergs melt.

Since icebergs are treated as point particles, the iceberg drift models are mostly suitable for modeling smaller icebergs drifting across large distances, and as such iceberg drift models have mostly been used to represent icebergs smaller than 3.5km on a global scale [Jongma et al , 2009; Martin and Adcroft , 2010; Marsh et al , 2015]. These models are not suitable for modeling larger tabular icebergs, which feel the ocean over many grid cells, depress the ocean surface and change circulation patterns [Stern et al , 2016]. They also not suitable for studying the local effects that icebergs have on the surrounding ocean. For this reason, tabular icebergs ($L > 5\text{km}$) are currently not represented in the iceberg drift models used in climate models, even though observations suggest that tabular icebergs account for the vast majority of the total Southern Hemisphere icebergs mass [Tournadre et al , 2016].

The ice shelf cavity models and iceberg drift models described above have been developed separately from one another, and have not been designed to be used together in a physically consistent way. As such, it has not been possible to model the calving of tabular icebergs away from an ice shelf, which is an important part of the Antarctic climate system. The goal of this study is to develop a model which combines features of the ice shelf cavity models and the iceberg drift models, to create an ice shelf cavity model that is able to calve tabular icebergs. To do this, we create an ice shelf model out of Lagrangian elements which are ‘bonded’ together by numerical bonds. In this framework, icebergs do not get created when a calving event takes place (as in iceberg drift models), but rather the icebergs ‘break’ away from an existing ice shelf, thus changing the geometry of the ice shelf cavity. Modeling iceberg calving in a physically consistent way allows us to study the

₁₁₄ ocean response to iceberg detachment (see Figures 1 and Figures 2, for example). Also, by
₁₁₅ allowing icebergs protrude deep into the water column we can study the ocean dynamics
₁₁₆ around individual tabular icebergs (which was not possible in iceberg drift models).

₁₁₇ In all simulation in this study, the shape of the calving iceberg is prescribed. The
₁₁₈ question of how to correctly prescribe a calving law is undoubtably a very important
₁₁₉ question, which has rightfully received much attention in recent years [Benn et all , 2007;
₁₂₀ Alley et al , 2008; Levermann et al , 2012]. Bassis and Jacobs [2013], for example, used
₁₂₁ a DEM model to study the generation and propagation of cracks within an ice shelf (not
₁₂₂ coupled to a dynamic ocean model). In this study, we bypass the question of how to
₁₂₃ correctly calve icebergs or break bonds. Instead we focus on developing a framework to
₁₂₄ model the ocean to response to ice shelf breaking and the presence of tabular icebergs.
₁₂₅ This framework of representing ice shelves using a Lagrangian grid might be a step towards
₁₂₆ including giant tabular icebergs in climate models. Including ice fracture into this model
₁₂₇ will be a later step.

₁₂₈ The model developed in this study is referred to at the Lagrangian Iceberg/Ice Shelf
₁₂₉ Model (LIISM). Section 2 gives a description of many of the key aspects of the LIISM.
₁₃₀ Since this model is a new approach to modeling ice shelf cavities, we present many of
₁₃₁ the technical elements involved in constructing the model. Those readers who are more
₁₃₂ interested in the model capabilities, should skip directly to the model results in the later
₁₃₃ sections. In Section 3 and 4, the LIISM model is used to simulate the circulation beneath
₁₃₄ an idealized ice shelf. The LIISM model results are validated by comparing them to an
₁₃₅ existing ice shelf model. We then we move beyond the capabilities of the existing ice shelf

₁₃₆ model by allowing a piece of the ice shelf to break away becoming a tabular icebergs, and
₁₃₇ consider the ocean response to this calving event.

2. Model description

₁₃₈ In this section we describe many key elements of the LIISM. The LIISM is a
₁₃₉ Lagrangian/particle-based model in that the objects of the model are Lagrangian ele-
₁₄₀ ments. Each element represents a mass of ice which is floating in the ocean, and has a
₁₄₁ position, velocity, mass, and a set of dimensions, which can evolve in time. The motion of
₁₄₂ each element is determined by a momentum equation which is solved in the (Lagrangian)
₁₄₃ reference frame of the element. The elements are forced by oceanic and atmospheric
₁₄₄ forces, which are provided by the user or are determined by coupling the LIISM to an
₁₄₅ ocean/atmosphere model. The elements also interact with one another and can be bonded
₁₄₆ together to form larger structures. In different contexts, the LIISM elements can be
₁₄₇ thought to represent individual icebergs, sea ice flows, or, when the elements are bonded
₁₄₈ together, they can represent larger structures such as tabular icebergs or ice shelves. In
₁₄₉ this latter case, the LIISM model can be categorized as a discrete element model (DEM).

₁₅₀ The LIISM model is developed on the code base of an existing iceberg drift model
₁₅₁ [Martin and Adcroft , 2010; Stern et al , 2016]. When run with the correct set of runtime
₁₅₂ flags, the model runs as a traditional iceberg drift model.

2.1. Equations of motion

₁₅₃ The elements drift in the ocean, forced by atmosphere, ocean and sea-ice drag forces,
₁₅₄ as well as the Coriolis force and a force due to the sea surface slope. When these ice
₁₅₅ elements move alone (without interactions with other elements), they can be thought of

¹⁵⁶ as representation of small icebergs, and follow the same equations described in the iceberg
¹⁵⁷ drift model of Martin and Adcroft [2010] (based on the equations outlined in Bigg et al
¹⁵⁸ [1997]; Gladstone et al [2001]).

¹⁵⁹ In addition to the environmental forces, the elements in the LIISM model experience
¹⁶⁰ interactive forces due to the presence of other elements. Two types of interactive forces are
¹⁶¹ included between elements. The first force is repulsive force which is applied to elements
¹⁶² to prevent them from moving too close to one another. This repulsive force prevents
¹⁶³ icebergs from piling up on top of one another. The second interactive force is a force due
¹⁶⁴ to numerical ‘bonds’, and is only applied if two elements are ‘bonded’ together. When
¹⁶⁵ two elements are bonded, each element feels an attractive force that prevents the elements
¹⁶⁶ from moving too far apart from one another. The interactive forces between two bonded
¹⁶⁷ elements are defined such that in the absence of other forces the elements come to rest
¹⁶⁸ adjacent to one another, with no overlap of the iceberg areas.

The momentum equation for each element is given by

$$M \frac{D\vec{u}}{Dt} = \vec{F}_A + \vec{F}_W + \vec{F}_R + \vec{F}_C + \vec{F}_{SS} + \vec{F}_{SI} + \vec{F}_{IA}, \quad (1)$$

¹⁶⁹ where $\frac{D}{Dt}$ is the total (Lagrangian) derivative, M is the mass of the element, \vec{u} is the
¹⁷⁰ velocity of the element, and the terms on the right hand side give the forces on the
¹⁷¹ element due to air drag (\vec{F}_A), water drag (\vec{F}_W), sea ice drag (\vec{F}_{SI}), Coriolis force (\vec{F}_C),
¹⁷² wave radiation force (\vec{F}_R), sea surface slope (\vec{F}_{SS}), and interactions with other elements
¹⁷³ (\vec{F}_{IA}). The environmental forces are the same as those presented in Martin and Adcroft
¹⁷⁴ [2010], and are provided for completeness in Appendix A. The details of the interactive
¹⁷⁵ forces are provided in below.

2.2. Interactive Forces

The interactive force on an element is calculated by adding together the interactions with all other elements, such that the interactive force on element i , $(\vec{F}_{IA})_i$ is given by:

$$(F_{IA})_i = \sum_{j \neq i} (F_{IA})_{ij}, \quad (2)$$

where $(F_{IA})_{ij}$ is the force on element i by element j . Both bonded and repulsive interactions are modeled using elastic stresses with frictional damping. The elastic component of the force is a function of the distance between the two elements, while the frictional damping force depends on the relative velocity of the two elements.

To describe the forces between two elements, we begin by introducing some notation.

Let \vec{x}_i , \vec{x}_j be the positions of elements i and j . The distance between elements i and j is

$$d_{ij} = |\vec{x}_i - \vec{x}_j|. \quad (3)$$

We then define the interaction diameter of an element by

$$D_i = 2\sqrt{\frac{A_i}{\pi}}, \quad (4)$$

where A_i is the planar surface area of element i . Using this, we define the critical interactive length scale,

$$L_{ij} = \frac{D_i + D_j}{2}, \quad (5)$$

which governs interactions between elements i and j . Repulsive forces are only applied when $d_{i,j} < L_{i,j}$, while bonded forces are only applied when $d_{i,j} > L_{i,j}$ and a bond exists between element i and j . Bond and repulsive forces are designed to such that in the absence of other forces, bonded particles will settle in an equilibrium position where elements are separated by the critical interaction length scale $L_{i,j}$.

To aid in notation, we define a bond matrix B_{ij} such that $B_{ij} = 1$ if elements i and j are bonded together and $B_{ij} = 0$ otherwise. Using this notation, the interactive force $(\vec{F}_{IA})_{ij}$ on an element i by an element j is given by

$$(\vec{F}_{IA})_{ij} = \begin{cases} (\vec{F}_e)_{ij} + (\vec{F}_d)_{ij} & \text{if } d_{ij} \leq L_{ij} \\ (\vec{F}_e)_{ij} + (\vec{F}_d)_{ij} & \text{if } d_{ij} > L_{ij} \text{ and } B_{ij} = 1 \\ 0 & \text{if } d_{ij} > L_{ij} \text{ and } B_{ij} = 0 . \end{cases} \quad (6)$$

$(\vec{F}_e)_{ij}$ and $(\vec{F}_d)_{ij}$ are the elastic and frictional damping components of the interactive force between elements i and j. The elastic force $(\vec{F}_e)_{ij}$ between elements is given by

$$(\vec{F}_e)_{ij} = -\kappa_e \left(d_{i,j} - L_{i,j} \right) T_{i,j} \vec{r}, \quad (7)$$

where $\vec{r} = \frac{(\vec{x}_i - \vec{x}_j)}{|\vec{x}_i - \vec{x}_j|}$ is the directional unit vector between the position of element i and j,

and κ_e is the spring constant, and $T_{i,j}$ is the minimum of the thickness of elements i, j.

We choose $(\vec{F}_b)_{ij}$ proportional to $T_{i,j}$ (the minimum thickness of elements i and j) so the formulation of interactive forces has the desired property that it obeys Newton's 3rd Law (i.e.: $(\vec{F}_{IA})_{ij} = -(\vec{F}_{IA})_{ji}$). This is in contrast to some other DEM models in the literature (e.g. Li et al [2014]). The minimum thickness is preferred to the average thickness, since this means that the for two bonded elements a fixed distance apart, acceleration due to elastic forces is bounded, even when the thickness of one of the elements approaches zero.

The frictional damping force has components that damp both the relative radial velocity and relative transverse velocities of the two elements. If \vec{r}^\perp is the direction vector perpendicular to \vec{r} , and $P_{\vec{r}}$ and $P_{\vec{r}^\perp}$ are the projection matrices that project onto \vec{r} and \vec{r}^\perp respectively, then the frictional damping force is given by

$$(\vec{F}_d)_{ij} = \left(-c_r P_{\vec{r}} - c_t P_{\vec{r}^\perp} \right) \cdot (\vec{u}_i - \vec{u}_j) \quad (8)$$

Here c_r and c_t are the radial and transverse drag coefficients. For the simulation below, we set $c_r = 2\sqrt{\kappa_e}$ and $c_t = \frac{1}{4}c_r$ so that the radial elastic force is critically damped, and the

¹⁹⁵ transverse damping is sub critical. The damping forces are implemented using an implicit
¹⁹⁶ time stepping scheme, to avoid stability issues for very small elements (details found in
¹⁹⁷ Appendix B).

¹⁹⁸ The effectiveness of the repulsive forces can be seen in Figure 3 which shows an un-
¹⁹⁹ coupled simulation where ice elements drift westward into a bay, and eventually come to
²⁰⁰ rest with minimal overlap between elements. The effectiveness of the numerical bonds is
²⁰¹ demonstrated in Figure 4 tabular icebergs (constructed from many ice elements bonded
²⁰² together) and individual icebergs (unbonded elements) drift together towards a convex
²⁰³ coast line. When the tabular icebergs arrive at the coast, they bump into the coastline
²⁰⁴ and begin to rotate, influencing the paths of the other icebergs. In this example we see
²⁰⁵ that modeling large structures using small elements bonded together, allows us to achieve
²⁰⁶ large-scale structure and rotational motion, without having to include an equation for the
²⁰⁷ angular momentum of the elements (as discussed in Jakobsen [2001]).

2.3. Element geometry and packing

²⁰⁸ Elements are packed differently depending on the shape of the elements. For all simula-
²⁰⁹ tions in this study, we use elements whose surface areas are equally-sized regular hexagons.
²¹⁰ In order to pack these elements together, the hexagonal elements are initially arranged in
²¹¹ a staggered lattice, with each element bonded to the adjacent elements (see Figure 5a).
²¹² In this arrangement, each element (away from the edges) is bonded to six other elements.
²¹³ The bonds between elements form a pattern of equilateral triangles, which give the larger
²¹⁴ structure rigidity.

²¹⁵ Some experiments were also performed using rectangular elements, arranged in a reg-
²¹⁶ ular (non-staggered) lattice. In this case, each element forms four bonds with adjacent

elements. However, the resultant structures were found to be much less rigid and tended to collapse when sufficient forces was applied. For this reason, hexagonal elements were preferred.

2.4. Ocean-ice and ice-ocean coupling

The LIISM model is coupled to the ocean model via a two-way synchronous coupling, meaning that ocean model fields are passed to the LIISM model and the LIISM model fields are passed back to the ocean model at every time step. Passing fields between the two models involves interpolating fields between the Eulerian grid of the ocean model and the ‘Lagrangian grid’ of the LIISM model (i.e.: onto the ice elements).

The coupling from the ocean model to the LIISM model is straight forward: at every time step, the ocean mixed layer temperature, salinity, velocity and sea-ice concentration are passed from the ocean model to the LIISM model, to be used in the momentum and thermodynamics equations of the ice elements. Within the LIISM model, the ocean model fields are interpolated onto the Lagrangian grid using a bilinear interpolation scheme. The LIISM model is not sensitive to the chosen interpolation scheme.

The coupling in the other direction, from the LIISM model to the ocean model, is more complex. The LIISM model influences the ocean by: (i) applying a pressure to the ocean surface, (ii) applying a heat, salinity and mass flux to the ocean, associated with ice melting, and (iii) affecting the upper ocean boundary condition by applying a no slip boundary condition and frictional velocity beneath the ice. Fields from the LIISM model are interpolated from the Lagrangian grid to the Eulerian ocean grid before they are passed to the ocean model. Since the LIISM model applies large pressures to the ocean surface, the ocean model is sensitive to the interpolation scheme used to map the

²³⁹ LIISM fields to the ocean grid. Sudden jumps to the ocean surface pressure can trigger
²⁴⁰ tsunamis within the ocean model, making the ocean model become unstable.

²⁴¹ The interpolation of the LIISM fields onto the ocean grid is done in a way that is
²⁴² consistent with the shape of the elements in the LIISM model (see Section 2.3). Fields
²⁴³ are ‘spread’ to the ocean model by exactly calculating what fraction of an element’s
²⁴⁴ surface area lies in a particular grid box, and dividing the field in proportion to this
²⁴⁵ fraction. For example, consider an element which has a hexagonal surface area in the
²⁴⁶ LIISM model, which is positioned such that it intersects four ocean grid cells (Figure
²⁴⁷ 5b). In this situation, the mass of the element is divided between these four ocean cells
²⁴⁸ in proportion to the overlap area between the hexagonal element and the grid cell (this
²⁴⁹ fraction is shown by the colors in 5b). An advantage of this approach is that there are no
²⁵⁰ jumps in pressure as an element moves from one grid cell to another.

²⁵¹ The numerical calculation of the intersection between hexagons and the ocean grid is
²⁵² simplified by dividing the hexagon into 6 equilateral triangles. This method allows for the
²⁵³ intersection to be found even when the hexagon is not aligned with the grid. The LIISM
²⁵⁴ model can be run using hexagonal or rectangular elements.

²⁵⁵ The field-spreading scheme is coded with the restriction that an element’s area can only
²⁵⁶ intersect a maximum of four ocean grid cells at a time. A consequence of this is that this
²⁵⁷ sets a limit on the maximum size of elements that can be represented using this model,
²⁵⁸ i.e.: the longest horizontal dimension of an ice element must be smaller than the ocean
²⁵⁹ grid spacing. Larger ice structures are constructed by bonding together smaller elements.

2.5. Thermodynamics

260 The ice elements decay according to a number of melt parameterizations. As the ice
261 elements melt, their mass decreases, and the appropriate salt, mass and heat fluxes are
262 passed to the ocean. In this section we described the melt parametrization for bonded,
263 unbonded and partially bonded elements.

264 As mentioned above, ice elements which do not interact with other elements are modeled
265 identically to the point particle icebergs described in Martin and Adcroft [2010]. These
266 elements melt according to three semi-empirical parametrization for melt commonly used
267 in previous iceberg studies [Gladstone et al , 2001; Martin and Adcroft , 2010]. Three
268 types of iceberg melting are used: basal melt, M_b , melt due to wave erosion, M_e and melt
269 due to buoyant convection, M_v . M_e and M_v are applied to the sides of the ice element,
270 while M_b is applied at the ice element base. The details of M_b . M_v and M_e are given in
271 Appendix A.

272 When multiple elements are bonded together to form larger structures, it is no long
273 appropriate to use the parameterizations for melt developed for individual point-particle
274 icebergs. An element which is completely surrounded by other elements, is meant to
275 represent a piece of ice in the middle of a large structure, and hence will not experience
276 a melt at its sides due to wave erosion or buoyant convection. Also, the iceberg basal
277 melt rate, M_b described above is based on boundary layer theory of flow past a finite
278 plate, and is only appropriate for basal surfaces where the distance from the leading edge
279 is sufficiently small [Eckert , 1950; Weeks and Campbell , 1973]. For an element in the
280 interior of large structures, the distance from the edge of the structure is large, and so
281 using M_b for the basal melt is not appropriate. Instead, the basal melt, M_s is determined

²⁸² using the three equation model for basal melt, which is a typical melting parametrization
²⁸³ beneath used beneath ice shelves [Holland and Jenkins , 1999].

When using both individual elements and bonded elements in the same simulation, we determine which melt rate parameterizations to use based on the amount of bonds that each element has. An element which is in the center of a large structure will form the maximum number of bonds, while unbonded elements form zero bonds. If maximum number of bonds that an element can form (given the shape of the element) is N_{max} , and the number bonds that an element has is N_b , then the side melt and bottom melt for that element are given by

$$M_{side} = \frac{(N_{max} - N_b)}{N_{max}}(M_v + M_e) \quad (9)$$

and

$$M_{bottom} = \frac{(N_{max} - N_b)}{N_{max}}M_b + \frac{N_b}{N_{max}}M_s \quad (10)$$

²⁸⁴ respectively. In this way, elements with no bonds, melt like point particle icebergs, ele-
²⁸⁵ ments at the center of large structures melt like ice shelves, and elements at the sides of
²⁸⁶ large structures have a combination of iceberg side and basal melt, and ice shelf melt.

2.6. Algorithms and computational efficiency

²⁸⁷ Including interactions between elements leads to an increase in the computational com-
²⁸⁸ plexity of the model. In this subsection we comment on some of the algorithmic proce-
²⁸⁹ dures that have been used to increase the computational efficiency. Readers who are not
²⁹⁰ interested in this more technical side of the model should skip this section.

2.6.1. Time stepping

292 The ice elements in the LIISM model are advected using a semi-implicit velocity Verlet
293 time-stepping scheme. The velocity verlet time stepping scheme is commonly used in DEM
294 models in video games because it is computational efficient and has desirable stability
295 properties [Jakobsen , 2001]. This time stepping scheme was preferred to the Runge-
296 Kutta 4, which was used in the iceberg model of Martin and Adcroft [2010] since, the
297 Verlet time stepping only requires one calculation of the interactive forces per time step
298 (while the Runge-Kutta scheme requires the interactive forces to be calculated four times).
299 Since the calculation of the interactive forces is one of the most computationally expensive
300 part of the algorithm, the Verlet scheme leads to a significant increase in the speed of the
301 model. We note that the Verlet scheme used in the LIISM contains a small modification
302 of the original (fully explicit) velocity Verlet time stepping scheme in that damping terms
303 are treated implicitly (which increases the numerical stability). The details of this time
304 stepping schemed are outline in Appendix B.

305 2.6.2. Interactions and Bonds

306 At every time step, we calculate the force on each element due to interactions with every
307 other element. In principle, this involves order n^2 operations (for n elements). However,
308 since each element only has repulsive interactions with elements that are less than one
309 ocean grid cell away, and each element only has bonded interactions with a small number
310 of other elements, we are able to reduce the complexity of the system.

311 The complexity reduction is achieved by storing the element data in an efficient way
312 that prevents having to search through all element pairs to check if they are close to
313 one another or are bonded with one another. The data storage system works as follows:
314 pointers to the memory structures containing each element are stored in linked list data

315 structures, which allow elements to be added and removed from the lists easily without
316 restructuring the entire list. Instead of using one list for all the elements on a processor,
317 we use a separate linked list for each ocean grid cell. When an element moves between
318 ocean grid cells, it is removed from its original list and added to the list corresponding to
319 its new ocean grid cell. Since the area of elements has to be smaller than the area of an
320 ocean grid cell, the critical interaction critical interaction length scale (equation 5) is less
321 than the length of a grid cell. This means that elements only experience repulsive forces
322 with elements in the same ocean grid cell, or in one of the 8 adjacent cells. Limiting the
323 possible repulsive interactions to elements in the 9 linked lists substantially reduces the
324 computational time needed to calculate the total interactive force.

325 Bonded interactions are handled slightly differently. Each bond is assigned a piece of
326 memory. Each ice element contains a linked list of each of its bonds (typically up to six
327 bonds per element). At each time step, the code traverses the lists of bonded elements,
328 and adds a bonded force corresponding to these bond. The bonded force is only applied
329 if $\vec{r}_{i,j} > L_{ij}$, to avoid double counting an interaction. Having a list of bonds stored with
330 each element reduces the computational complexity of bonded interactions from order n^2
331 to order n. Handling bonded attractive forces separately to the repulsive and non-bonded
332 forces means that we do not need to check whether two elements are bonded, which further
333 increases the computational efficiency.

334 **2.6.3. Parallelization and halos**

335 The LIISM model runs on multiple processors in parallel. When elements move from
336 an ocean cell on one processor to an ocean cell on a second processor, the memory has to
337 be passed from one processor the next, added and removed to the appropriate lists and

338 the memory has to be allocated and deallocated correctly. Element interactions across
339 the edge of processors are handled using computational halos. A computational halo is a
340 copy of the edge of a one processor which is appended to the edge of a second processor,
341 so that the first processor can ‘see’ the second processor during a time step. Before a
342 time step, elements at the edges of each processor are copied onto the halos of adjacent
343 processors so that they can be used in calculating the interactive forces. After each time
344 step, these halos are removed, and the process is repeated. These halo updates are one
345 of the most computationally expensive parts of the LIISM model.

346 Keeping track of pairs of bonded elements that move across a processor edge requires
347 a lot of book keeping since bonds have to be severed and reconnected. Details of how
348 the bonds are broken and reconnected across processor boundaries are provided in Ap-
349 pendix C.

3. Experiment Setup

350 The introduction of Lagrangian elements, numerical bonds and interpolation schemes
351 between the Eulerian and Lagrangian grids (discussed in Section 2) means that we are
352 now able to model ice shelf cavities which undergo large calving events. We demonstrate
353 this capability by performing numerical experiments with the LIISM model coupled to
354 the MOM6 ocean model [reference].

3.1. MISOMIP configuration

355 In order for our (pre-calving) simulations to be easily comparable to previous models
356 of ice shelf cavities, we use an experimental setup based on the configuration created for
357 the Marine Ice Ocean Modeling Inter-comparison Project (MISOMIP) [Asay-Davis et al

, 2016]. The MISOMIP configuration was developed as a standardize configuration to allow for the comparison between various ocean-ice coupled models. The configuration consists of an idealized ice shelf in a rectangular domain. The domain is $L_x = 80\text{km}$ wide and $L_y = 480\text{km}$ long, and contains an ice shelf which is grounded on the south side of the domain and has an ice front at $y=650\text{km}$. The ice thickness and bottom topography of this setup are shown in Figure 6a and 6b respectively, with the grounding line position drawn in for reference. The configuration is the same as that of the Ocean0 setup in the MISOMIP, with three changes made:

1. The ‘calving criteria’ used in the MISOMIP study (which states that all points in the ice shelf with thickness less than 100m are set to zero thickness) has not been used.
2. The ice shelf has been thickened on the flanks of the domain, so that the latitude of the grounding line increases away from the center of the ice shelf.
3. The ice shelf is configured to be symmetric about its center line. This was achieved by using the average of the left and right flank of the ice shelf thickness.

These three changes were made in order to make the circulation beneath the ice shelf easier to interpret.

The LIISM model is coupled to the MOM6 ocean model. The ocean model is run in layered mode, with a horizontal resolution of $\Delta x = 2 \text{ km}$, and 36 vertical layers. Ocean parameters are as specified in the MISOMIP configuration [Asay-Davis et al , 2016], and are shown in Table 1. The simulation is initially at rest, with horizontally uniform initial ocean temperature (Figure S4a) and salinity profiles that vary linearly between specified surface and bottom values. The initial surface temperature and salinity are $T_t = -1.9^\circ\text{C}$ and $S_t = 33.8 \text{ psu}$, respectively. The initial temperature and salinity at the depth H_{ocean}

are $T_b = 1.0^\circ\text{C}$ and $S_b = 34.7 \text{ psu}$. The maximum ocean depth is $H_{ocean} = 720 \text{ m}$. A sponge layer is used on the northern boundary of which relaxes back to the initial temperature and salinity with a relaxation time scale of $\tau = 0.1 \text{ days}$. Melting is set to zero for cells where the ocean column thickness is less than 10m to avoid using more energy to melt ice than is present in the water column.

3.2. Initializing Lagrangian elements:

Ice elements in the LIISM model are set to be hexagonal and are arranged in a regular staggered lattice (as discussed in Section 2.3). The apothem of the gridded hexagons are initially set to $A = 0.85 \text{ km}$. Recall that the element size must be smaller than the ocean grid spacing (i.e.: $2A < \Delta x$). Gaps along the boundary are filled in with using smaller elements so that the total ice shelf area is preserved. The initial mass of the ice elements is determined by a preprocessing inversion step, which is the inverse of the 'mass-spreading' interpolation procedure discussed in Section 2.3.

Figure 6c shows what the ice shelf draft would be if the draft were calculated from the mass of elements in each ocean grid cell without spreading an elements mass across neighboring cells (i.e.: treating elements as point masses). Figure 6b shows the draft after spreading the mass across grid cells. When the mass spreading interpolation scheme is not used, grid artifacts seen in the ice shelf draft (Figure 6c). The grid artifacts are much reduced when the mass spreading interpolation is used (Figure 6b).

3.3. Static ice shelf experiment

In the first experiment, we use a static ice shelf where the velocity of all ice elements is set to zero. In this experiment, the ice shelf is thermodynamically active and is able to

401 ‘melt’ but has a constant thickness (as was done in the Ocean0 setup in the MISOMIP
402 [Asay-Davis et al , 2016]). In this setup, ice shelf melting generates a temperature and
403 salinity flux into the ocean, but does not change the thickness of the ice shelf. This can
404 be thought to represent an ice shelf in dynamic equilibrium where the melt is exactly
405 balanced ice shelf advection.

406 Results of the static ice shelf experiment using the LISSM model are compared to the
407 results from an existing Eulerian ice shelf model [Goldberg et al , 2012], coupled to the
408 same ocean model. The simulations in the Lagrangian and Eulerian are compared after
409 5 years of models time.

3.4. Tabular iceberg calving

410 In the next set of experiments, we demonstrates capabilities of the LIISM model that
411 can not be performed by traditional Eulerian ice shelf models. These simulations model a
412 large tabular iceberg being calved from the edge of the ice shelf. The tabular iceberg drifts
413 in the ocean, submerged in the water column, where it influences the ocean circulation.

414 The tabular iceberg simulations are initialized using the ocean state from the end of the
415 static ice shelf experiment (after 5 years). For these situations, all ice elements initially
416 within a 15km radius of the center of the ice front are allowed to move freely while the other
417 ice elements continue to be held stationary. The three tabular iceberg simulations are
418 performed:

419 **1. Tabular iceberg with fixed velocity:**

420 In this simulation, the velocity of the non-stationary elements is fixed to $u=0\text{m/s}$,
421 $v=0.01\text{m/s}$. This simulation allows us to study the response of the ocean to distur-

⁴²² bance caused by a tabular iceberg moving through the water (with an fixed velocity).
⁴²³ This simulation is not fully coupled since the velocity of the elements is prescribed.

⁴²⁴ 2. Tabular iceberg with bonded elements:

⁴²⁵ All non-stationary ice elements are bonded together by the numerical bonds. This ex-
⁴²⁶ periments is fully-coupled in that the ice elements are driven the ocean, and the pressure
⁴²⁷ exerted by the ice elements drives ocean flow. In order to make the iceberg drift away
⁴²⁸ from the ice shelf, we imposed a zonal wind stress of $\tau_x = 0.1 \frac{N}{m^2}$.

⁴²⁹ 3. Tabular iceberg with unbonded elements:

⁴³⁰ This simulation is identical to the bonded elements simulation, except that all the numer-
⁴³¹ ical bonds are broken, so that the elements are free to move away from one another.

4. Results

4.1. Static ice shelf experiment

⁴³² Comparison of LIISM and Eulerian ice shelf model

⁴³³ The results from coupled ocean-ice simulation in the MISOMIP configuration using LIISM
⁴³⁴ are compared to the results using an Eulerian ice shelf model in the same configuration.
⁴³⁵ The ice draft in the Eulerian ice shelf model is initialized using the field shown in Figure
⁴³⁶ 6b. Figures S2 show the time-averaged melt rates of both the Lagrangian and Eulerian
⁴³⁷ ice shelf models, averaged over the first 5 years of the simulation.

⁴³⁸ The melt rates of the Eulerian and Lagrangian models are very similar with slight
⁴³⁹ difference showing up at the grounding line and ice front (Figure S2). The slight difference
⁴⁴⁰ at the grounding line are a result of the fact that elements in the LIISM model are smaller
⁴⁴¹ than a grid cell in length. This means that ice element near the grounding line may be
⁴⁴² ungrounded in the LIISM model, while the grid cell is considered grounded in the Eulerian

443 model. At the ice front, the Eulerian model has a straight ice front, while the LIISM model
444 has a staggered ice front, which is a result of the staggered hexagonal packing.

445 The small changes in melt at the grounding line and ice front drive slight changes to the
446 circulation beneath the ice shelf, which in turn lead to small difference in the temperature
447 and salinity profiles over time. This is seen by comparing the time-averaged ocean salinity
448 profiles for the Lagrangian and Eulerian ice shelves (Figure S1) and also by comparing the
449 the time-averaged barotropic stream function of the two simulations (see Figures S6) and
450 in the supplementary material). The differences between the Eulerian and Lagrangian
451 simulations are small compared to the wide spread of difference seen in the MISOMIP
452 inter comparison. This is unsurprising, since the LIISM and Eulerian ice shelves are
453 coupled to the same ocean model and pass similar fields to the ocean model.

454 The similarity of the Lagrangian and Eulerian ice shelf models shows that the LIISM
455 model coupled to an ocean model is able to model sub ice shelf cavities as well as the
456 Eulerian model does. This is a good starting point for moving beyond the capabilities of
457 the Eulerian model.

4.2. Tabular iceberg calving

458 Tabular iceberg with fixed velocity

459 The fixed iceberg velocity calving experiment demonstrates that the model is able to
460 simulate a tabular iceberg being calved from an ice shelf. After the iceberg calves, it
461 moves northwards away from the ice shelf with a prescribed velocity. After the iceberg
462 has calved away from the ice shelf, we observed a warming of the surface waters near the
463 near the ice front and iceberg edge. This surface warming is caused by an upwelling of the
464 warmer waters from beneath the ice shelf and iceberg. As the icebergs drifts away from

the ice front, these warmer waters remain in the wake of the iceberg (Figures 2). The signature of upwelling water in the wake of a drifting tabular iceberg bears some similarity to satellite observations of streaks of increased ocean color near to tabular iceberg in the Southern Ocean [reference], suggesting that the increased productivity around iceberg may be driven by upwelling water delivering nutrients to the surface. The motion of the iceberg also drives barotropic velocities through out the water column, which disturb the initial stratification of the water column (Figures 1).

Fully coupled tabular iceberg

The necessity of bonds between ice elements is demonstrated by comparing two simulations where an iceberg calves, and is allowed to evolve freely with the flow. In the Bonded simulation, the elements in the calved iceberg are bonded together, while in the Unbonded simulation the all bonds between elements in the tabular iceberg are broken.

In the Bonded simulation, the ice element in the tabular iceberg remain close to one another, and the tabular iceberg retains its shape (Figure 10a,c). The elements are forced by the melt-water-driven current at the ice front, which moves towards the north-west (see Figure S3 in the supplementary material). This current, together with the Coriolis force, cause the iceberg to rotate before moving away from the ice shelf (Figure 10a).

In the Unbonded simulation, the ice elements in tabular iceberg are not constrained to move together. Instead, the elements spread out and drift towards the north-west for the same reason discussed above. Since the ice elements are not closely, packed together, they apply a smaller pressure to the ocean surface, spread over a larger area (Figure 10c). The type of behavior could be relevant in simulating ice shelf disintegrations, rather than tabular iceberg calving.

5. Discussion

- 488 1) How do we get this into a big coupled climate model - what is still needed? Bond
 489 breaking, ice growing 2) Mention lagrangian sea ice

6. Appendix A

6.1. Environmental forces on ice elements

The non-interactive forces on an ice element are as described in [Martin and Adcroft , 2010], and are repeated here for completeness. The force on an element due to air (a), ocean (o) and sea ice (si) drag are given by

$$(\vec{F}_a) = \rho_a(0.5c_{a,v}WF + c_{a,h}LW)|\vec{u}_a - \vec{u}|(\vec{u}_a - \vec{u}), \quad (11)$$

$$(\vec{F}_o) = \rho_o(0.5c_{o,v}W(D - T_{si})F + c_{o,h}LW)|\vec{u}_o - \vec{u}|(\vec{u}_o - \vec{u}), \quad (12)$$

$$(\vec{F}_{si}) = \rho_{si}(0.5c_{si,v}WT_{si}F + c_{si,h}LW)|\vec{u}_{si} - \vec{u}|(\vec{u}_{si} - \vec{u}). \quad (13)$$

490 Here ρ_a , ρ_o , ρ_{si} , are the density of air, ocean and sea ice, respectively. $c_{a,v}$, $c_{o,v}$ and $c_{si,v}$
 491 are the vertical drag coefficients with air, ocean and sea ice, while $c_{a,h}$, $c_{o,h}$ and $c_{si,h}$ are
 492 the respective horizontal drag coefficients. Here \vec{u}_a , \vec{u}_o , \vec{u}_{si} , are the velocities air, ocean
 493 and sea ice, respectively. L, W, T, F and D are the length, width, thickness, freeboard
 494 and draft of the ice element. The element thickness is related to the draft and freeboard
 495 by $T = F + D$ and $D = \frac{\rho}{\rho_o}T$, where ρ is the ice element density.

The wave radiation force (\vec{F}_R) is given by

$$\vec{F}_R = \frac{1}{2}\rho_o c_r g a \min(a, F) 2 \frac{WL}{W + L} \frac{\vec{v}_a}{|\vec{v}_a|} \quad (14)$$

where g is the acceleration due to gravity, a is the wave amplitude empirically related to the wind speed by $a = 0.010125|\vec{v}_a - \vec{v}_o|$, and c_{wd} is the wave drag coefficient defined as

$$c_{wd} = 0.06 \min \left(\max \left[0, \frac{L - L_c}{L_t - L_c} \right], 1 \right), \quad (15)$$

where $L_w = 0.32|\vec{v}_a - \vec{v}_o|^2$ is an empirical wave length, $L_c = 0.125L_w$ is the cutoff length, and $L_t = 0.25L_w$ is the upper limit.

The pressure gradient force is approximated as a force due to sea surface slope and given by

$$\vec{F}_{SS} = -Mg\vec{\nabla}\eta \quad (16)$$

where η is the sea surface height.

6.2. Melt rate parametrization

As discussed in Section 2.5, unbounded ice elements in the LIISM model decay according to parameterizations for iceberg decay typically used in iceberg drift models [Martin and Adcroft , 2010], while ice elements within larger ice structures have only a basal melt given by the three equation model [Holland and Jenkins , 1999] .

For unbonded ice elements, the element thickness decays at due to basal melt at a rate M_b , while the length and width of the elements decay as a result of melt due to wave erosion, M_e and melt due to buoyant convection, M_v . Following Martin and Adcroft [2010], the basal melt rate, wave erosion melt rate, and buoyant convection melt rate are parameterized by

$$M_b = 0.58|\vec{v} - \vec{v}_0|^{0.8} \frac{\tilde{T}_0 - \tilde{T}}{L^{0.2}} \quad (17)$$

$$M_e = \frac{1}{12}S_s \left(1 + \cos [\pi A_i^3] \right) \left(\tilde{T}_0 + 2 \right), \quad (18)$$

$$M_v = \left(7.62 \times 10^{-3} \right) \tilde{T}_0 + \left(1.29 \times 10^{-3} \right) \tilde{T}_0^2. \quad (19)$$

\tilde{T} is the effective iceberg temperature and is set to $\tilde{T} = 4^\circ\text{C}$, \tilde{T}_0 is the temperature at the top of the ocean, A_i is the sea ice area fraction, and S_s is the sea state, which is given by the Beaufort scale

$$S_s = \frac{2}{3} |\vec{u}_a - \vec{u}_o|^{\frac{1}{2}} + \frac{1}{10} |\vec{u}_a - \vec{u}_o| \quad (20)$$

503 All three melt rates are in units of meters per day.

504 For elements inside larger structures, the melt due to wave erosion and melt due to
 505 buoyant convection are set to zero, and the basal melt, M_s is given by the standard three
 506 equation model [Holland and Jenkins , 1999].

7. Appendix B

7.1. Modified Verlet Algorithm

507 The LIISM model uses a version velocity verlet algorithm, which has been modified
 508 to allow part of the forcing to be calculated implicitly. The traditional velocity verlet
 509 algorithm is commonly used in molecular dynamics, as it is simple to implement, second
 510 order accurate and computationally efficient [Swope et al , 1982; Omelyan et al , 2002].

511 Here we modify the tradition scheme to allow for the drag forces to be modeled implicitly,
 512 which prevents large accelerations for element's whose mass approaches zero. To do
 513 this, we modify the traditional verlet algorithm to include both an implicit and explicit
 514 acceleration, $a(t) = a_{exp}(t) + a_{imp}(t)$. The explicit acceleration, $a_{exp}(t)$ includes all forcing
 515 terms which depend only on the previous time step, while the implicit acceleration, $a_{imp}(t)$
 516 includes forcing terms which depend on the current time step (in particular the drag and
 517 Coriolis forces).

Using a time step of Δt and the notation $t_{n+1} = t_n + (\Delta t)$, the modified velocity verlet scheme can be written as:

$$1) \quad x(t_{n+1}) = x(t_n) + u(t_n)\Delta t + \frac{1}{2}\Delta t^2 \left(a_{exp}(t_n) + a_{imp}(t_n) \right).$$

2) Calculate $a_{exp}(t_{n+1})$ and $a_{imp}(t_{n+1})$

$$3) \quad u(t_{n+1}) = u(t_n) + \frac{\Delta t}{2} \left(a_{exp}(t_n) + a_{exp}(t_{n+1}) \right) + (\Delta t)a_{imp}(t_{n+1})$$

This scheme reduces to the traditional velocity verlet when a_{imp} is set to zero. Note that

at step 2, $a_{exp}(t_{n+1})$ is an explicit function of $x(t_{n+1})$ and other qualities evaluated at time t_n , while $a_{imp}(t_{n+1})$ additionally depends on $u(t_{n+1})$ (and needs to be solved implicitly).

For this reason, steps 2 and 3 need to be solved simultaneously, as described in the next section.

In equation (1), the forces due to ocean drag, atmospheric drag and sea ice drag are treated implicitly. The force due to sea surface slope and wave radiation are treated explicitly. The Coriolis term is handled using Crank-Nicolson scheme so that half of the effect is implicit and half is explicit. The elastic part of the interactive forces is treated explicitly, while the interactive damping is handled semi-implicitly in that the drag force on element A by element B depends on the velocity of elements A and B evaluated at time t_{n+1} and t_n , respectively.

7.2. Solving for the velocity implicitly

Since this modified scheme contains some forcing terms which are handled implicitly, steps 2 and 3 need to be solved together. We demonstrate how this is done, using a simplified one-dimensional version of equation (1), neglecting the atmospheric drag, sea ice drag and Coriolis force, so that the only implicitly treated term is the ocean drag. We also define an explicit force F_{exp} , which accounts for all forces not proportional the

element velocity. With these simplifications, the implicit and explicit accelerations are

$$a_{exp} = \frac{1}{M}(\vec{F}_{exp}) \quad (21)$$

$$a_{imp} = \frac{1}{M}(F_W) \quad (22)$$

The ocean drag force at time t_{n+1} is modeled (mostly) implicitly as

$$F_W(t_{n+1}) = c_w|u_w(t_n) - u(t_n)|(u_w(t_n) - u(t_{n+1})) \quad (23)$$

Step 3 of the modified velocity verlet scheme can be rewritten by introducing an intermediate velocity u^* , which only depends on the velocity and acceleration at time t_n ,

$$u^*(t_n) = u(t_n) + \frac{1}{2}(\Delta t)a(t_n). \quad (24)$$

Using this, the updated velocity (Step 3) can be written

$$u(t_{n+1}) = u^*(t_n) + \frac{\Delta t}{2}a_{exp}(t_{n+1}) + (\Delta t)a_{imp}(t_{n+1}). \quad (25)$$

Including the forcing terms into this equations gives

$$u(t_{n+1}) = u^*(t_n) + \frac{\Delta t}{2M}(F_{exp}(t_{n+1})) + \frac{\Delta t}{M} \left(c_w|u_w(t_n) - u(t_n)|(u_w(t_n) - u(t_{n+1})) \right) \quad (26)$$

Solving for $u(t_{n+1})$ in terms of quantities which only depend on the previous time step

gives

$$u(t_{n+1}) = \frac{u^*(t_n) + \frac{\Delta t}{2M}(F_{exp}(t_{n+1})) + \frac{\Delta t}{M} \left(c_w|u_w(t_n) - u(t_n)|(u_w(t_n)) \right)}{\left(1 + \frac{\Delta t}{M}c_w|u_w(t_n) - u(t_n)| \right)} \quad (27)$$

Once the $u(t_{n+1})$ has been found, it can be used to calculate the explicit and implicit accelerations, which are required for the next time step.

Finally, we note that the the drag term (equation 23) is not entirely implicit, since the element velocity inside the absolute value is evaluated at time t_n , rather than at time

539 t_{n+1} . This is done so that we can solve for the updated velocity exactly. One consequence
540 of this is that it gives rise to a small oscillation in the element velocity. This oscillation is
541 addressed by using a predictive corrective scheme: once you have solved for a first guess
542 of the velocity at time t_{n+1} , this estimate of the velocity is used to update the estimate
543 of the drag force (i.e.: inside the absolute value signs). Using the updated drag, you can
544 now repeat the process described above to find an improved estimate of the velocity. We
545 found that two iterations were sufficient to remove the unwanted oscillation.

546 The procedure described in this section is easily extended to include more forcing terms
547 and two dimensions (where it involves inverting a 2×2 matrix).

8. Appendix C

548 Connecting bonds across processor boundaries

549 When a bonded element moves off the edge of a processor, the bond needs to be bro-
550 ken. When the element is copied into the halo of the processor, the bond needs to be
551 reconnected.., and then reconnected when the element is copied back

552 The basics of the bond bookkeeping work as follows. Consider an element A and an
553 element B that are bonded together. As mentioned above, each element has a copy of
554 the bond which is stored with the element. Let A-B be the bond stored by element A,
555 and B-A be the bond stored by element B. Bond A-B contains a pointer which points to
556 element B and bond B-A contains a pointer which points to element A.

557 Consider a situation where element A and B are originally on Processor 1, and then
558 element B moves to Processor 2. When this occurs, the memory assigned to element B
559 on processor 1 is removed, and is allocated on Processor 2. This means that the pointer
560 to element B in bond A-B (stored in element A on Processor 1) is no longer assigned.

561 Similarly, the pointer to element A in bond B-A (stored in element B on Processor 2) is
562 no longer assigned. Before the next time step, a halo update occurs, so that there is
563 a copy of element A in the halo of Processor 2 and a copy of element B in the halo of
564 Processor 1. After the halo update, the bonds A-B and B-A have to be reconnected on
565 both Processor 1 and 2. To aid in reconnecting the bonds, a copy of the grid cell number
566 of element B is stored in the bond A-B and a copy of the grid cell number of element A
567 is stored in the bond B-A. We refer to this as the ‘most recent address’. Before a bond
568 is moved from one processor to another, the ‘most recent address’ is updated, so that the
569 bond can be reconnected later. To reconnect bond A-B on Processor 1 (for example), we
570 find the most recent address of element B, and search through the list of elements in the
571 grid cell corresponding to the most recent address of element B until element B is found.
572 The pointer to element B in bond A-B is reassigned and the bond is said to be connected.

573 Once all bonds are reconnected, a bond quality control is done where we loop through
574 all bonds and check that they are working properly. To check that a bond is working
575 properly is a four step process. For example, consider the bond A-B stored in element A
576 on Processor 1. To check the quality of this bond A-B, we use the following four steps:

- 577 1. Check that the pointer to element B is assigned on bond A-B (stored on element
578 A).
- 579 2. Check that the corresponding bond B-A exists on element B.
- 580 3. Check that a pointer to element A exists in this bond B-A.
- 581 4. Check that the element A which is being pointed to is the same element A where
582 you started.

583 All four of these tests must pass in order to make sure that the memory is correctly
584 assigned. A useful tool in this process is that each element is assigned a unique number
585 so that elements are easily identified.

9. Possibly add

9.1. Lagrangian sea ice mode

586 The addition of interactive forces between elements, means that the LIISM model can
587 be used as a Lagrangian sea ice model, following [Li et al, 2014]. In this formulation, each
588 element represents a collection of sea ice flows.

9.2. Orientation

589 We can get the orientation of iceberg by considering the bonds that they form.

590 9.2.1. DEM vs SPH

591 Note that there is some ambiguity in the literature about the definition of a Discrete
592 Element Model. In one view, to qualify as a Discrete Element Model since we do not
593 evolve the angular momentum of the elements. Since elements are allows to overlap
594 briefly, this method could be considered an example of a Smooth Particle Hydrodynamics
595 model. This same repulsive force is similar to that used by [Li et al] in the context of sea
596 ice interactions.

References

- 597 Asay-Davis, X. S., S. L. Cornford, B. K. Galton-Fenzi, R. M. Gladstone, G. H. Gudmundsson, D. M. Holland, P. R. Holland, and D. F. Martin (2016), Experimental design for
598 three interrelated marine ice sheet and ocean model intercomparison projects: MIS-
599 MIP v. 3 (MISMIP+), ISOMIP v. 2 (ISOMIP+) and MISOMIP v. 1 (MISOMIP1).
600
601 *Geoscientific Model Development* 9, no. 7: 2471.
- 602 Arrigo, K. R., G. L. van Dijken, D. G. Ainley, M. A. Fahnestock, and T. Markus (2002).
603 Ecological impact of a large Antarctic iceberg. *Geophys. Res. Lett.*, 29(7).
- 604 Alley, R. B., H. J. Horgan, I. Joughin, K. M. Cuffey, T. K. Dupont, B. R. Parizek, S.
605 Anandakrishnan, and J. Bassis (2008), A simple law for ice-shelf calving. *Science* 322,
606 no. 5906, 1344-1344.
- 607 Bassis, J. N., and S. Jacobs (2013), Diverse calving patterns linked to glacier geometry.
608 *Nature Geoscience*, 6(10), 833-836.
- 609 Benn, D. I., C. R. Warren, and R. H. Mottram (2007). Calving processes and the dynamics
610 of calving glaciers. *Earth-Science Reviews*, 82(3), 143-179.
- 611 Bigg, G. R., Wadley, M. R., Stevens, D. P., and Johnson, J. A. (1997), Modelling the
612 dynamics and thermodynamics of icebergs. *Cold Regions Science and Technology*, 26(2),
613 113-135.
- 614 Biddle, L. C., J. Kaiser, K. J. Heywood, A. F. Thompson and A. Jenkins (2015), Ocean
615 glider observations of iceberg-enhanced biological productivity in the northwestern Wed-
616 dell Sea, *Geophys. Res. Lett.*, 42, 459465.
- 617 De Rydt, J., and G. H. Gudmundsson (2016), Coupled ice shelf?ocean modeling and
618 complex grounding line retreat from a seabed ridge. *J. of Geophys. Res.: Earth Surface*,

- 619 121(5), 865-880.
- 620 Dunne, J.P., J.G. John,, A.J. Adcroft, S.M. Griffies, R.W. Hallberg, E. Shevliakova,
621 R.J. Stouffer, W. Cooke, K.A. Dunne, M.J Harrison, and J.P. Krasting (2012), GFDL's
622 ESM2 global coupled climate-carbon Earth System Models. Part I: Physical formulation
623 and baseline simulation characteristics. *J. of Climate*, 25(19), 6646-6665.
- 624 Depoorter, M. A., J. L. Bamber, J. A. Griggs, J. T. M. Lenaerts, Stefan RM Ligtenberg,
625 M. R. van den Broek, and G. Moholdt (2013), Calving fluxes and basal melt rates of
626 Antarctic ice shelves. *Nature*, 502(7469), 89-92.
- 627 Determan J., Gerdes R. (1994), Melting and freezing beneath ice shelves: implications
628 from a three-dimensional ocean-circulation model. *Ann. Glaciol.*, 20, 413-419.
- 629 Dowdeswell, J. A., and J. L. Bamber (2007). Keel depths of modern Antarctic icebergs
630 and implications for sea-floor scouring in the geological record. *Marine Geology*, 243(1),
631 120-131.
- 632 Eckert, E. R. G. (1950). Introduction to the Transfer of Heat and Mass. McGraw-Hill.
- 633 Gladstone, R. M., G. R. Bigg, and K. W. Nicholls. (2001), Iceberg trajectory modeling
634 and meltwater injection in the Southern Ocean (19782012). *J. of Geophys. Res.: Oceans*,
635 106(C9), 19903-19915.
- 636 Goldberg, D. N., C. M. Little, O. V. Sergienko, A. Gnanadesikan, R. Hallberg, and M.
637 Oppenheimer (2012), Investigation of land ice?ocean interaction with a fully coupled
638 ice?ocean model: 1. Model description and behavior. *J. of Geophys. Res.: Earth Surface*,
639 117(F2).
- 640 Gladish, C. V., D. M. Holland, P. R. Holland, and S. F. Price (2012), Ice-shelf basal
641 channels in a coupled ice/ocean model. *J. of Glaciol.*, 58(212), 1227-1244.

- 642 Grosfeld K., R. Gerdes, J. Determan (1997), Thermohaline circulation and interaction
643 between ice shelf cavities and the adjacent open ocean. *J. Phys. Oceanogr.*, **102**, C7,
644 15959-15610.
- 645 Grosfeld, K., and H. Sandhger, (2004). The evolution of a coupled ice shelfocean system
646 under different climate states. *Global and Planetary Change*, 42(1), 107-132.
- 647 Holland D. M., Jenkins A. (2001), Adaptation of an isopycnic coordinate ocean model for
648 the study of circulation beneath ice shelves. *Mon. Wea. Rev.*, 129, 1905-1927.
- 649 Holland P. R. and D. L. Feltham (2006), The effects of rotation and ice shelf topography
650 on frazil-laden Ice Shelf Water plumes. *J. Phys. Oceanogr.*, 36, 2312-2327.
- 651 Holland, D. M., and A. Jenkins (1999), Modeling thermodynamic ice-ocean interactions
652 at the base of an ice shelf. *J. of Phys. Oceanogr.* 29.8, 1787-1800.
- 653 Hellmer H.H., Olbers D. J. (1989), A two-dimensional model for the thermohaline circu-
654 lation under an ice shelf. *Antarctic Science*, 1, 325- 336.
- 655 Jakobsen, T. (2001). Advanced character physics. In *Game Developers Conference*, Vol.
656 3.
- 657 Jenkins, A., P. Dutrieux, S. S. Jacobs, S. D. McPhail, J. R. Perrett, A. T. Webb, and
658 D. White (2010), Observations beneath Pine Island Glacier in West Antarctica and
659 implications for its retreat. *it Nature Geo.*, 3(7), 468-472.
- 660 Jacobs, S. S., A. Jenkins, C. F. Giulivi, and P. Dutrieux (2011). Stronger ocean circulation
661 and increased melting under Pine Island Glacier ice shelf. *Nature Geo.*, 4(8), 519-523.
- 662 Jongma, J. I., E. Driesschaert, T. Fichefet, H. Goosse, and H. Renssen (2009), The effect of
663 dynamic-thermodynamic icebergs on the Southern Ocean climate in a three-dimensional
664 model, *Ocean Modell.*, 26, 104113.

- 665 Lewis E.L. and R.G. Perkin (1986), Ice pumps and their rates. *J. of Geophys. Res.*, 91,
666 11756-11762.
- 667 Losch, M. (2008). Modeling ice shelf cavities in a z coordinate ocean general circulation
668 model. *J. of Geophys. Res.: Oceans*, 113(C8).
- 669 Li, B., H. Li, Y. Liu, A. Wang and S. Ji (2014), A modified discrete element model for
670 sea ice dynamics. *Acta Oceanologica Sinica*, 33(1), 56-63.
- 671 Lichéy, C., and H. H. Hellmer (2001). Modeling giant-iceberg drift under the influence of
672 sea ice in the Weddell Sea, Antarctica. *J. of Glaciol.*, 47(158), 452-460.
- 673 Levermann, A., T. Albrecht, R. Winkelmann, M. A. Martin, M. Haseloff, and I. Joughin.
674 (2012), Kinematic first-order calving law implies potential for abrupt ice-shelf retreat.
675 *The Cryosphere*, 6(2), 273-286.
- 676 Martin, T., and Adcroft, A. (2010), Parameterizing the fresh-water flux from land ice
677 to ocean with interactive icebergs in a coupled climate model. *Ocean Modelling*, 34(3),
678 111-124.
- 679 Marsh, R., V. O. Ivchenko, N. Skliris, S. Alderson, G. R. Bigg, G. Madec, A. T. Blaker
680 Y. Aksenov, B. Sinha, A.C. Coward, and J.L. Sommer (2015), NEMOICB (v1. 0):
681 interactive icebergs in the NEMO ocean model globally configured at eddy-permitting
682 resolution. *Geoscientific Model Development* 8, no. 5 (2015): 1547-1562.
- 683 MacAyeal D.R. (1984), Thermohaline Circulation Below the Ross Ice Shelf: A Conse-
684 quence of Tidally Induced Vertical Mixing and Basal Melting. *J. Geophys. Res.*, 89,
685 597-606
- 686 Nicholls K.W. (1996), Temperature variability beneath Ronne Ice Shelf, Antarctica, from
687 thermistor cables. *J. Phys. Oceanogr.*, 11, 1199-1210.

- 688 Nicholls KW, Østerhus S, Makinson K (2009), Ice-Ocean processes over the continental
689 shelf of the southern Weddell Sea, Antarctica: a review. *Rev. Geophys.* 47(3).
- 690 Omelyan, I. P., M. I. Mryglod, and R. Folk (2002), Optimized Verlet-like algorithms for
691 molecular dynamics simulations. *Physical Review E*, 65(5), 056706.
- 692 Rignot, E., S. Jacobs, J. Mouginot, and B. Scheuchl (2013), Ice-shelf melting around
693 Antarctica. *Science*, 341, no. 6143 (2013): 266-270.
- 694 Robinson, N. J., M. J. M. Williams, P. J. Barrett, and A. R. Pyne (2010), Observations of
695 flow and ice-ocean interaction beneath the McMurdo Ice Shelf, Antarctica, *J. Geophys.
696 Res.*, 115, C03025
- 697 Sergienko, O. V. (2013). Basal channels on ice shelves. *J. of Geophys. Res.: Earth Surface*,
698 118(3), 1342-1355.
- 699 Silva, T. A. M., Bigg, G. R., and Nicholls, K. W. (2006), Contribution of giant icebergs
700 to the Southern Ocean freshwater flux. *J. of Geophys. Res.: Oceans*, 111(C3).
- 701 Smith, K., B. Robison, J. Helly, R. Kaufmann, H. Ruhl, H., T. Shaw, and M. Vernet
702 (2007), Free-drifting icebergs: Hotspots of chemical and biological enrichment in the
703 Weddell Sea, *Science*, 317, 478482.
- 704 Stern, A. A., D. M. Holland, P. R. Holland, A. Jenkins and J. Sommeria (2014), The effect
705 of geometry on ice shelf ocean cavity ventilation: a laboratory experiment. *Experiments
706 in Fluids*, 55(5), 1-19.
- 707 Stern, A.A., Johnson, E., Holland, D.M., Wagner, T.J., Wadhams, P., Bates, R., Abra-
708 hamsen, E.P., Nicholls, K.W., Crawford, A., Gagnon, J. and Tremblay, J.E. (2015),
709 Wind-driven upwelling around grounded tabular icebergs. *J. of Geophys. Res.: Oceans*,
710 120(8), 5820-5835.

- 711 Stern, A. A., A. Adcroft, and O. Sergienko (2016), The effects of Antarctic iceberg calv-
712 ing?size distribution in a global climate model. *J. of Geophys. Res.: Oceans*, 121(8),
713 5773-5788.
- 714 Swope, W. C., H. C. Andersen, P. H. Berens, and K. R. Wilson (1982), A computer
715 simulation method for the calculation of equilibrium constants for the formation of
716 physical clusters of molecules: Application to small water clusters. *The Journal of
717 Chemical Physics* 76, no. 1, 637-649.
- 718 Tournadre, J., N. Bouvier, F. Girard-Ardhuin, and F. Remy (2016), Antarctic icebergs
719 distributions 1992-2014. *J. Geophys Res: Oceans*.
- 720 Vernet, M., et al. (2012), Islands of ice: Influence of free-drifting Antarctic icebergs on
721 pelagic marine ecosystems, *Oceanography*, 25(3), 3839
- 722 Weeks, W. F., and W. J. Campbell (1973). Icebergs as a fresh-water source: an appraisal.
723 *J. of Glaciol.*, 12(65), 207-233.

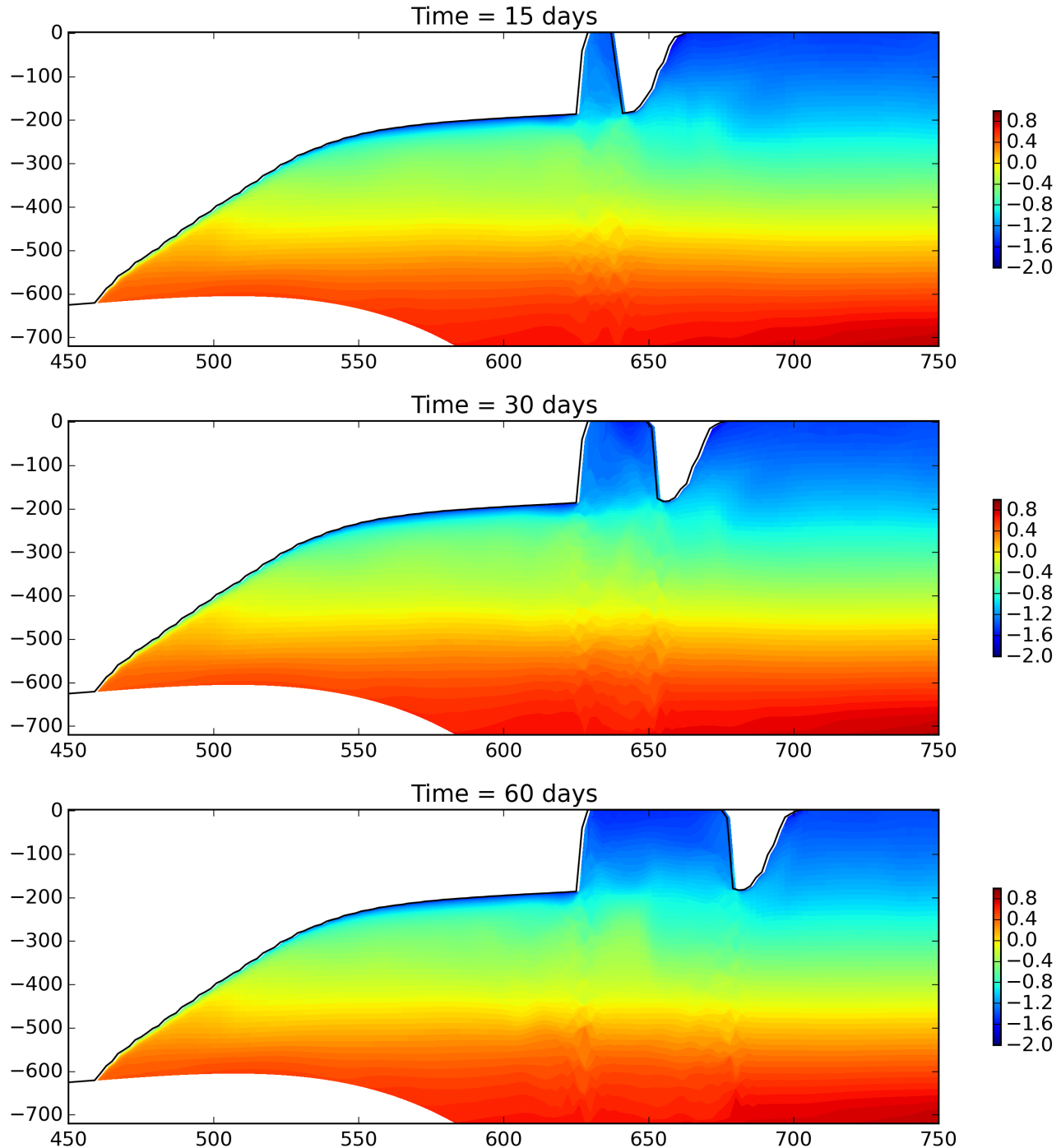


Figure 1. Temperature section at $y = \frac{L_y}{2}$ for the tabular iceberg calving with fixed velocity simulation (using the LIISM ice shelf) at time (a) $t=15$, (b) $t=30$, and (c) $t=60$ days.

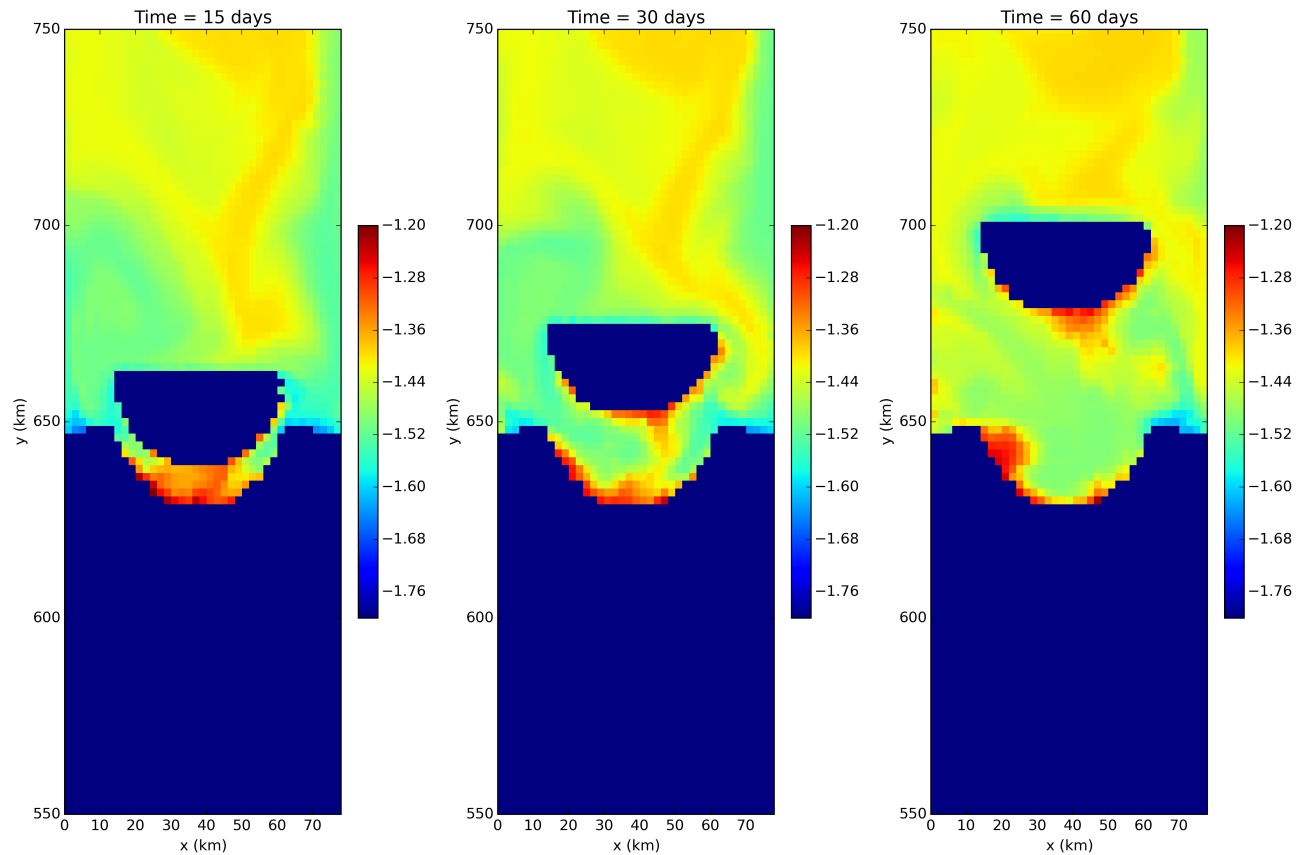


Figure 2. Sea surface temperature for the tabular iceberg calving with fixed velocity simulation at time (a) $t=15$, (b) $t=30$, and (c) $t=60$ days.

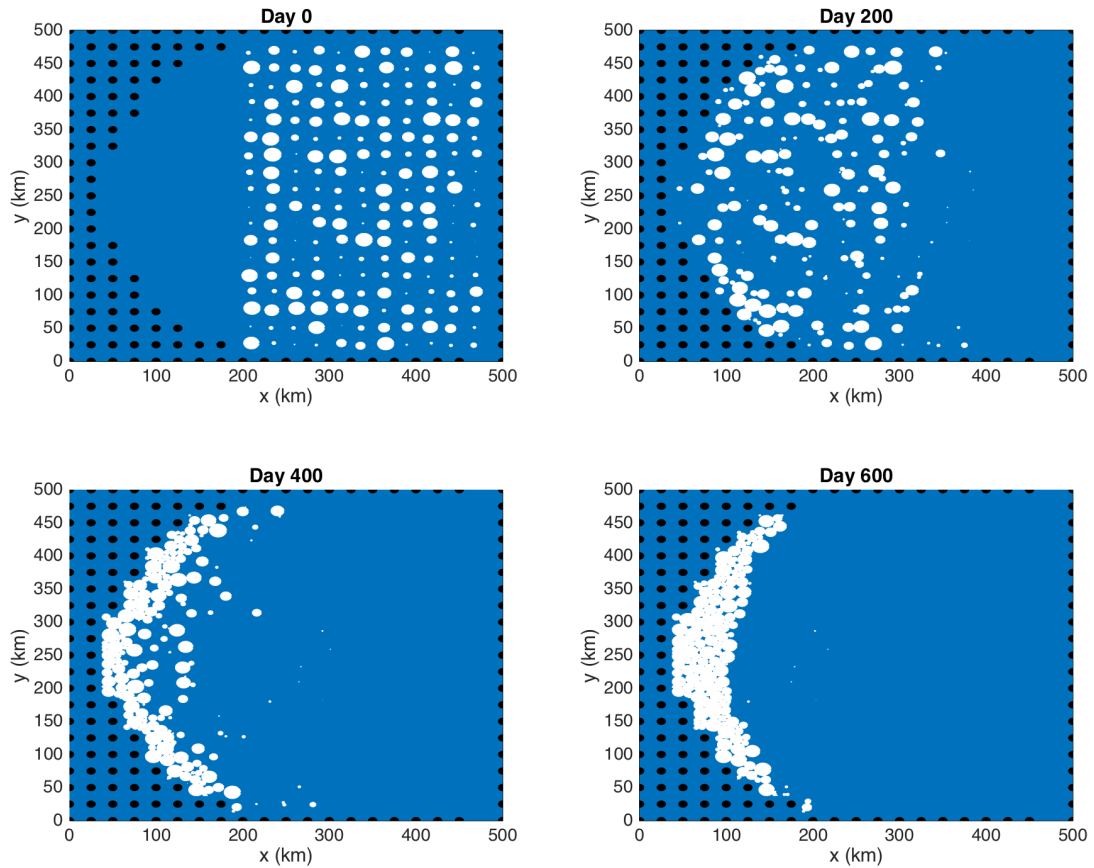


Figure 3. Positions of ice elements at time $t=0, 200, 400, 600$ days for the simulation. The size of the dots shows the surface area (and interaction diameter) of each ice element. Land points are shown by black circles.

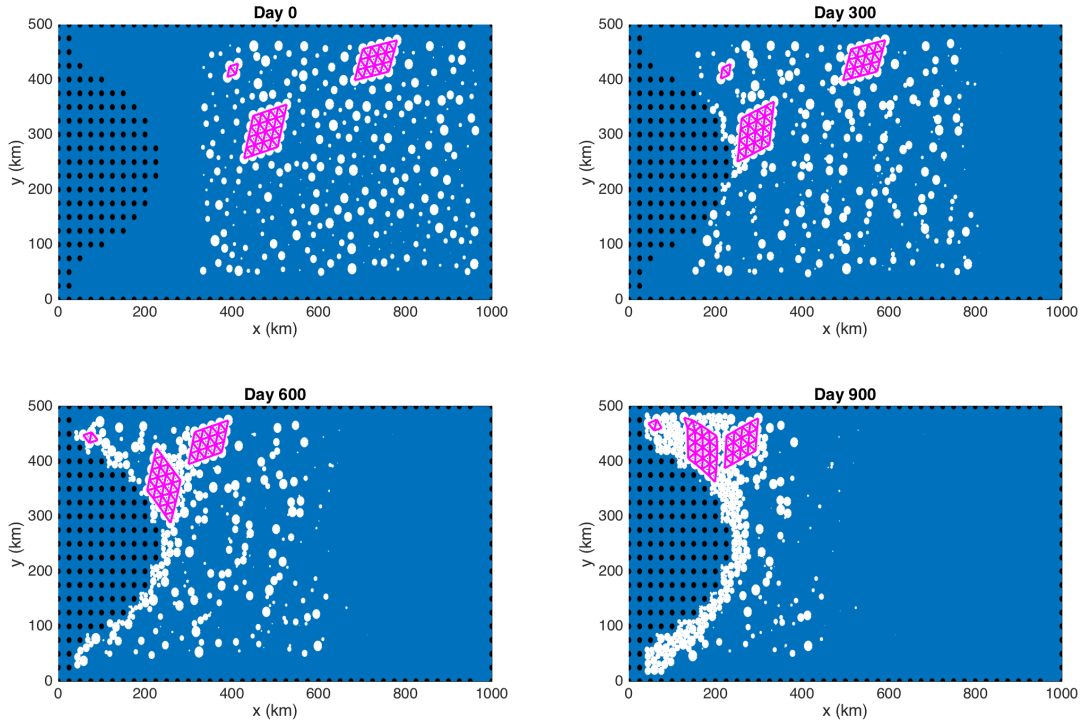


Figure 4. Positions of ice elements at time $t=0, 300, 600, 900$ days for the simulation. The size of the dots shows the surface area (and interaction diameter) of each ice element. Bonds between ice elements are plotted in magenta. Three tabular icebergs are shown, with 25, 16 and 4 elements respectively. Land points are shown by black circles.

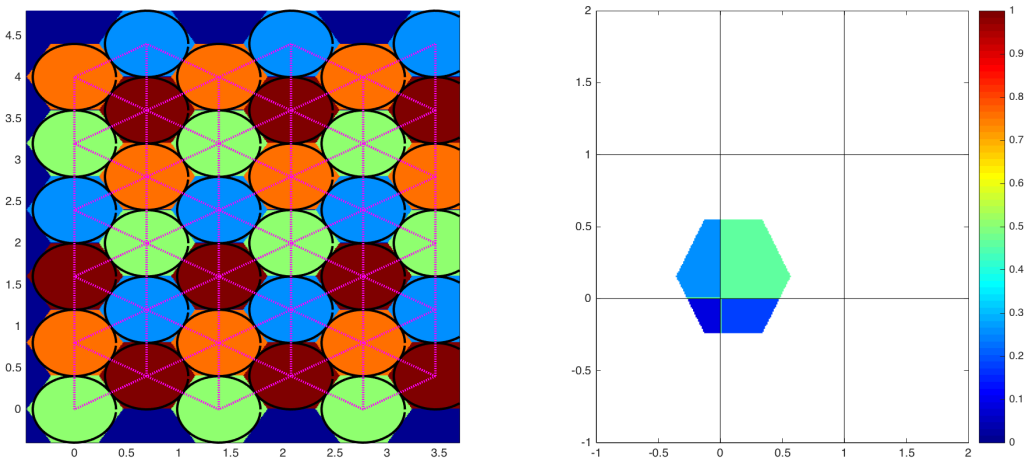


Figure 5. (a) Intersection of hexagonal element and ocean grid is used to find weights to spread LIISM properties to the ocean grid. (b) Hexagonal elements are initialized in a staggered lattice as shown. Adjacent elements are bonded together. The centers of bonded elements are plotted in pink. The element bonds form equilateral triangles which give the larger structure rigidity. The black circles shows to the interactive length scales used in element interactions.

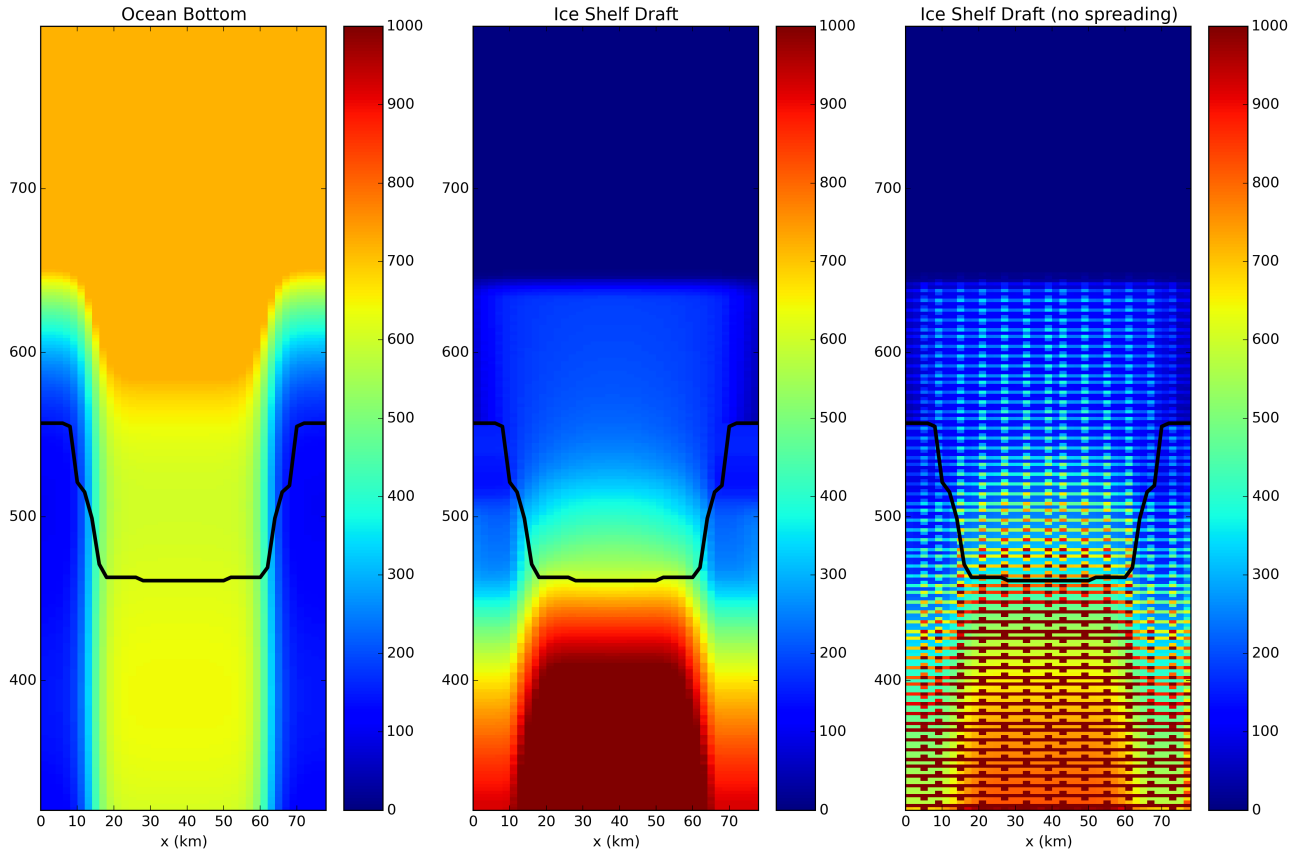


Figure 6. (a) Ocean bottom topography in ISOMIP configuration. (b) Ice shelf draft used in static shelf experiment. The ice draft is calculated from the ice mass in an ocean grid cell, which is found by spreading ice mass across ocean cells accounting for the size of each element (as explained in Section ?). (c) Same as in panel (b), except that the interpolation does not account for iceberg size, and instead treats elements as point masses.

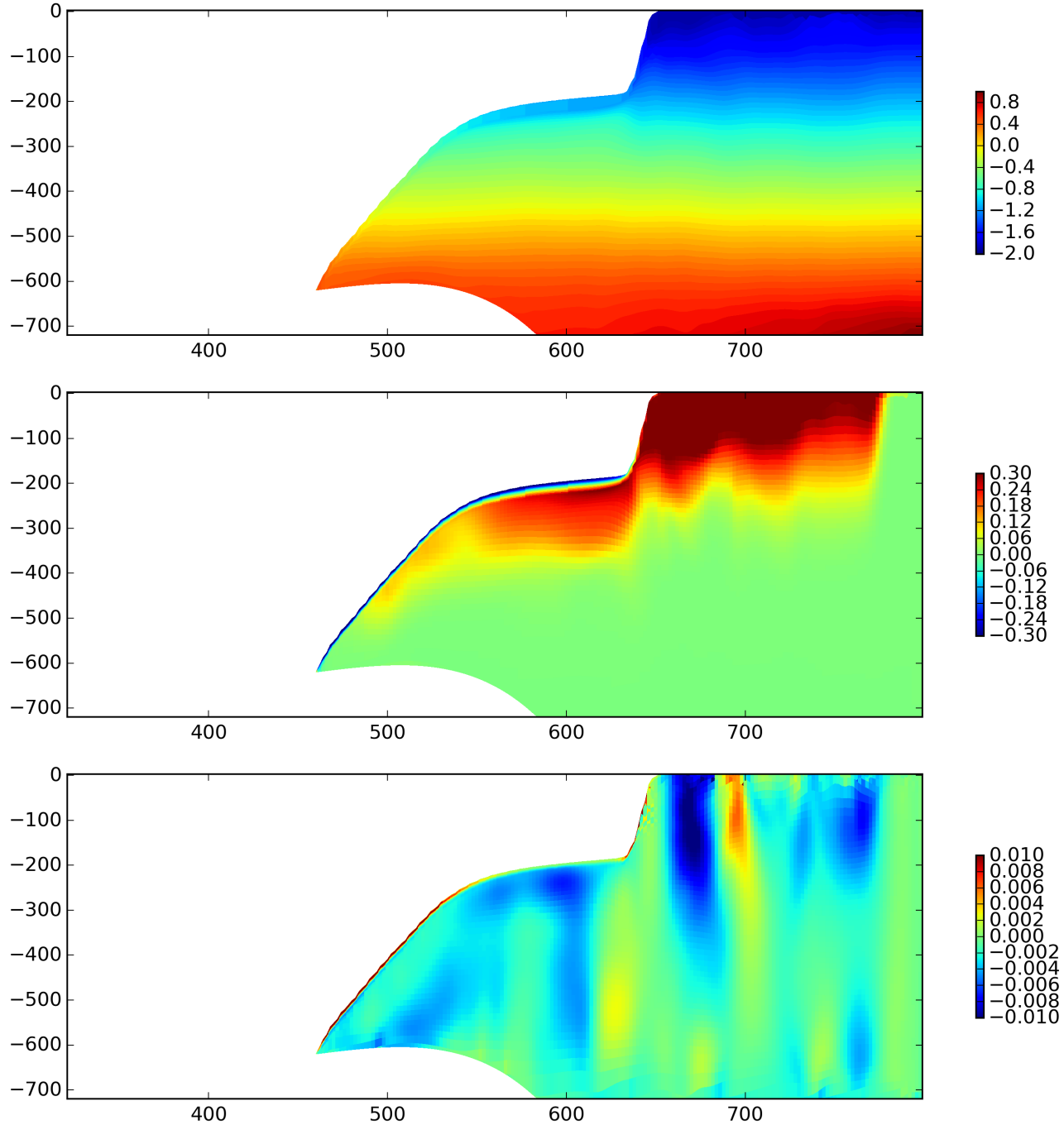


Figure 7. Results of the static ice shelf experiment using the LIISM model. Panels show a cross section of the (a) initial temperature field, (b) temperature anomaly after 5-years (relative to the initial field), and (c) meridional velocity after 5 years of simulation.

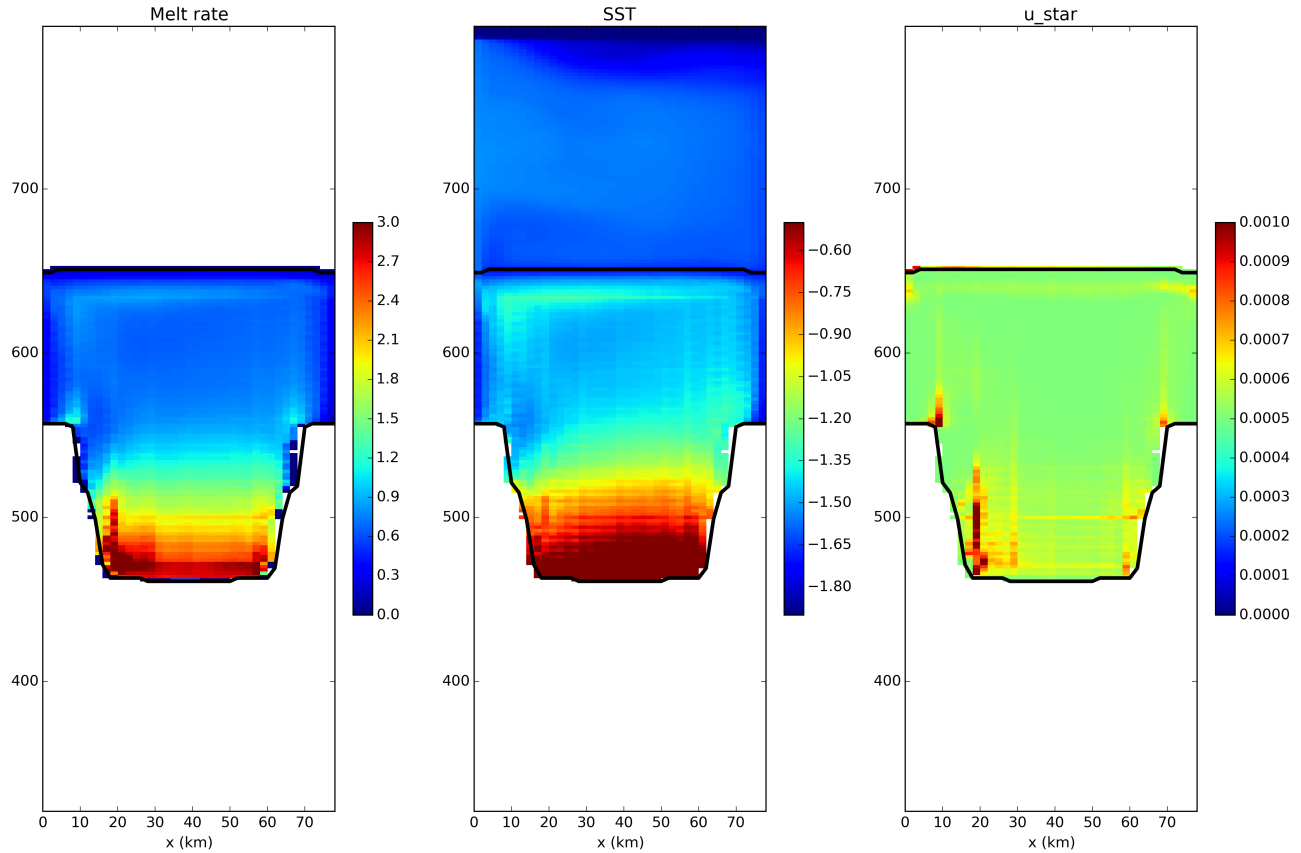


Figure 8. Results of the static ice shelf experiment using the LIISM model. The three panels show 5 year time average of the (a) melt rate, (b) ocean surface temperature and (c) u^* in the top layer of the simulation (at the surface or directly below the ice shelf).

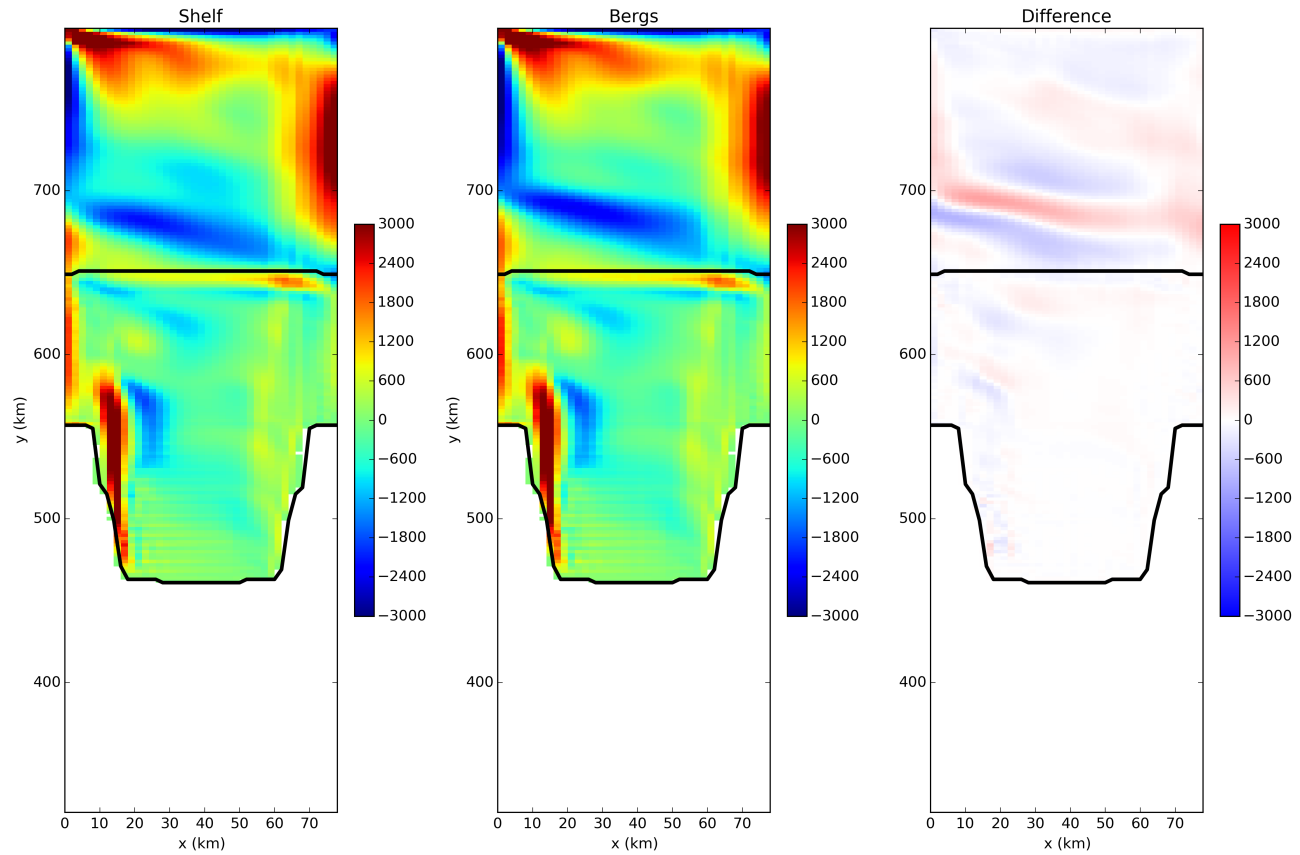


Figure 9. Comparison of Eulerian ice shelf model and Lagrangian Ice shelf model barotropic stream function

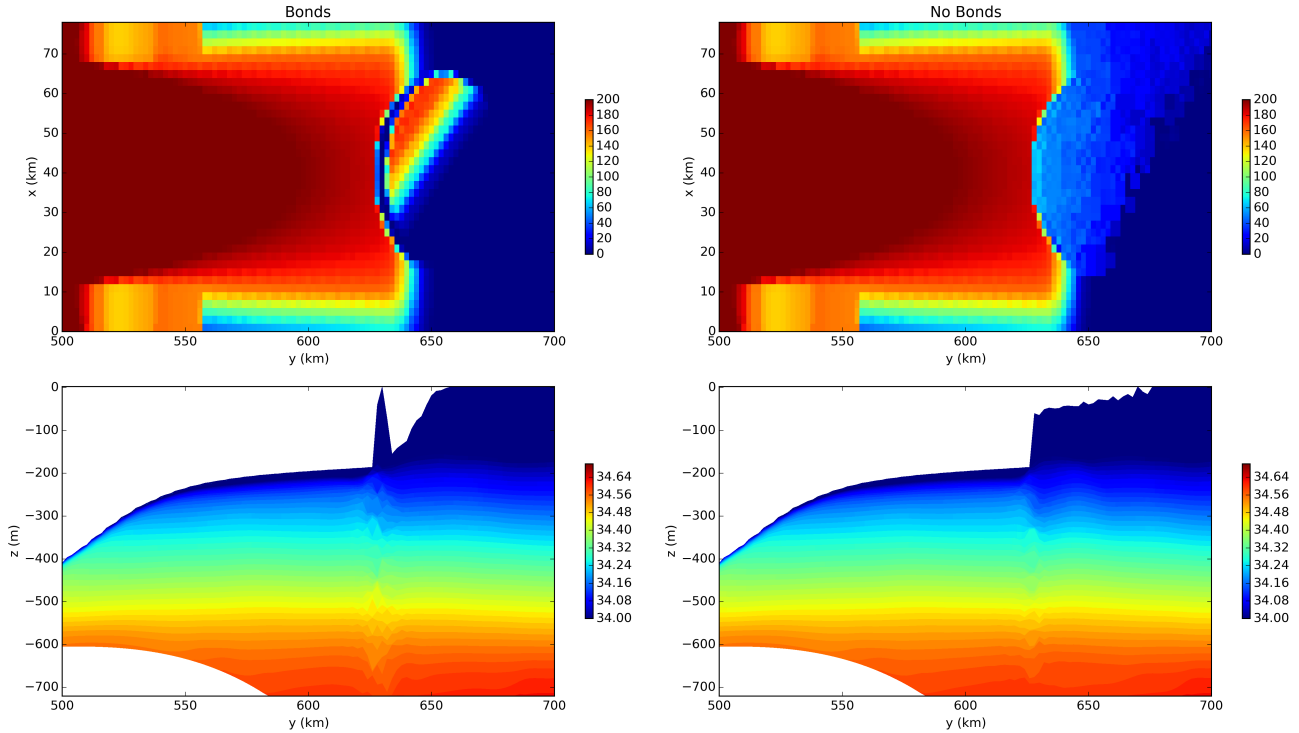


Figure 10. Calving of tabular iceberg with the LIISM model fully coupled to the ocean for simulations with and without bonds between ice elements. The top row show the aveage draft of ice above the ocean in each grid cell for the simulation (a) with and (b) without bonds. The bottom row shows the corresponding temperature section at $y = \frac{L_y}{2}$ for the simulation (a) with and (b) without bonds. All snapshots are taken at time $t= 30$ days.

10. Supplementary Figures

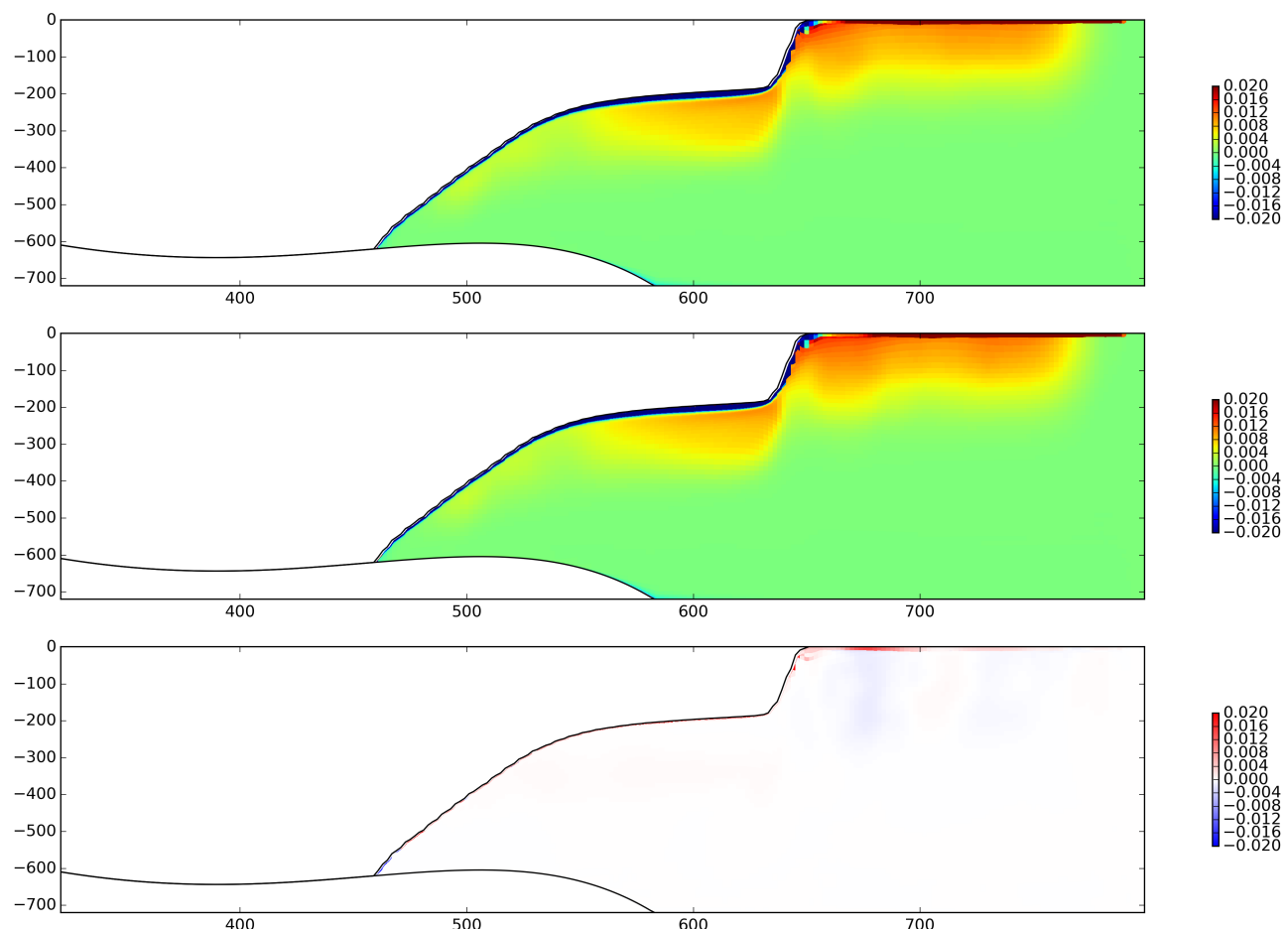


Figure S1. Comparison of Eulerian ice shelf model and Lagrangian Ice shelf model salinity fields.

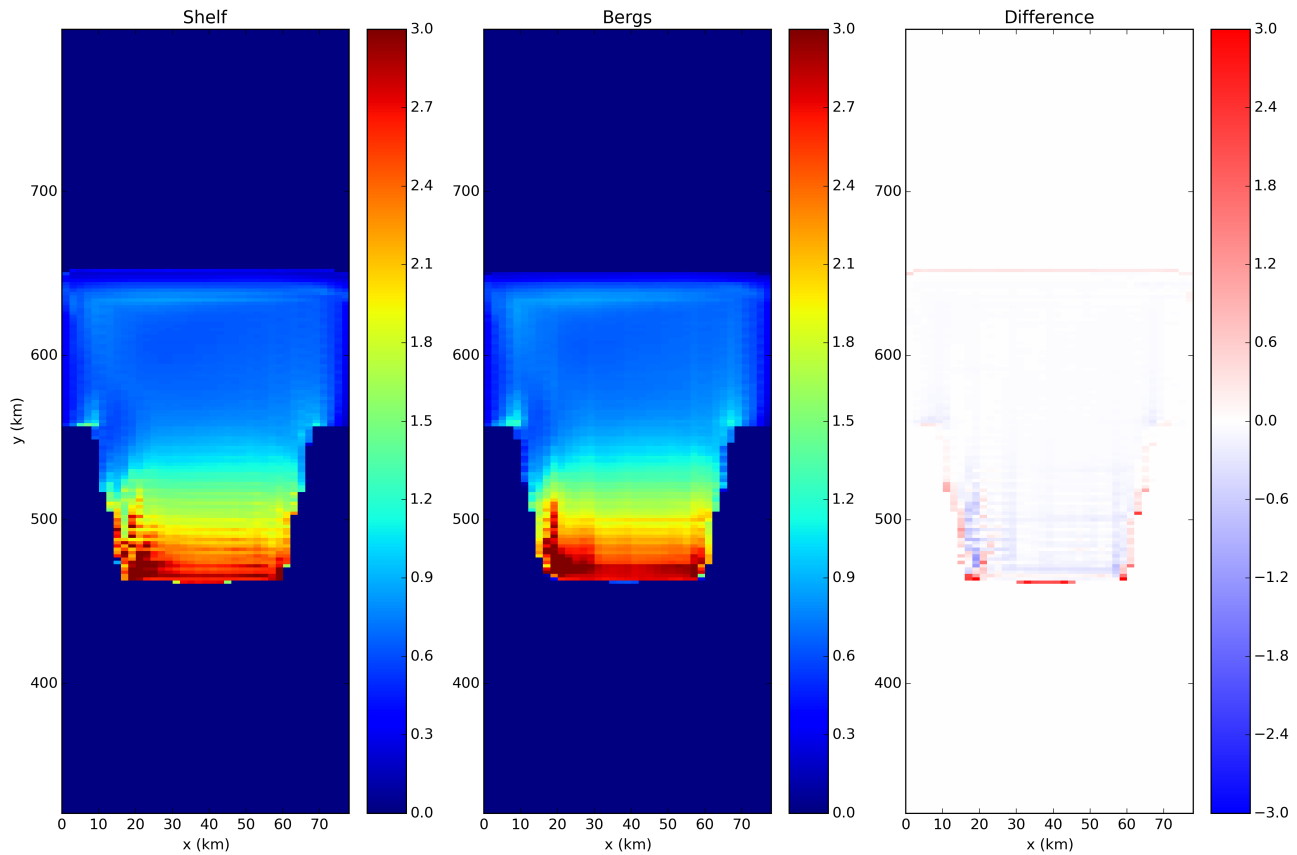


Figure S2. Comparison of Eulerian ice shelf model and Lagrangian Ice shelf model melt fields.

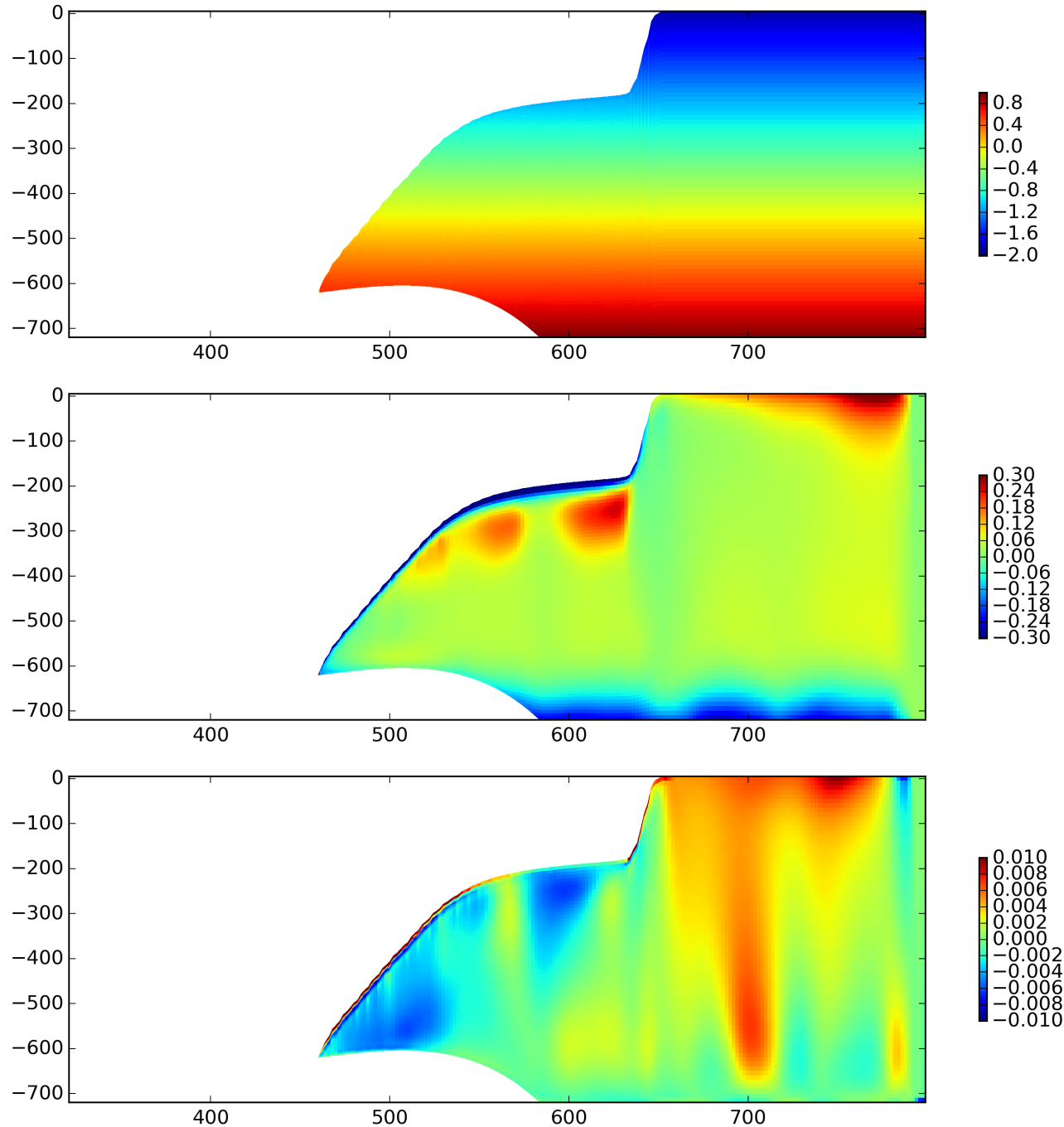


Figure S3. ALE z , Results of the static ice shelf experiment using the LIISM model. Panels show a cross section of the (a) initial temperature field, (b) temperature anomaly after 5-years (relative to the initial field), and (c) meridional velocity after 5 years of simulation.

11. ALE versions

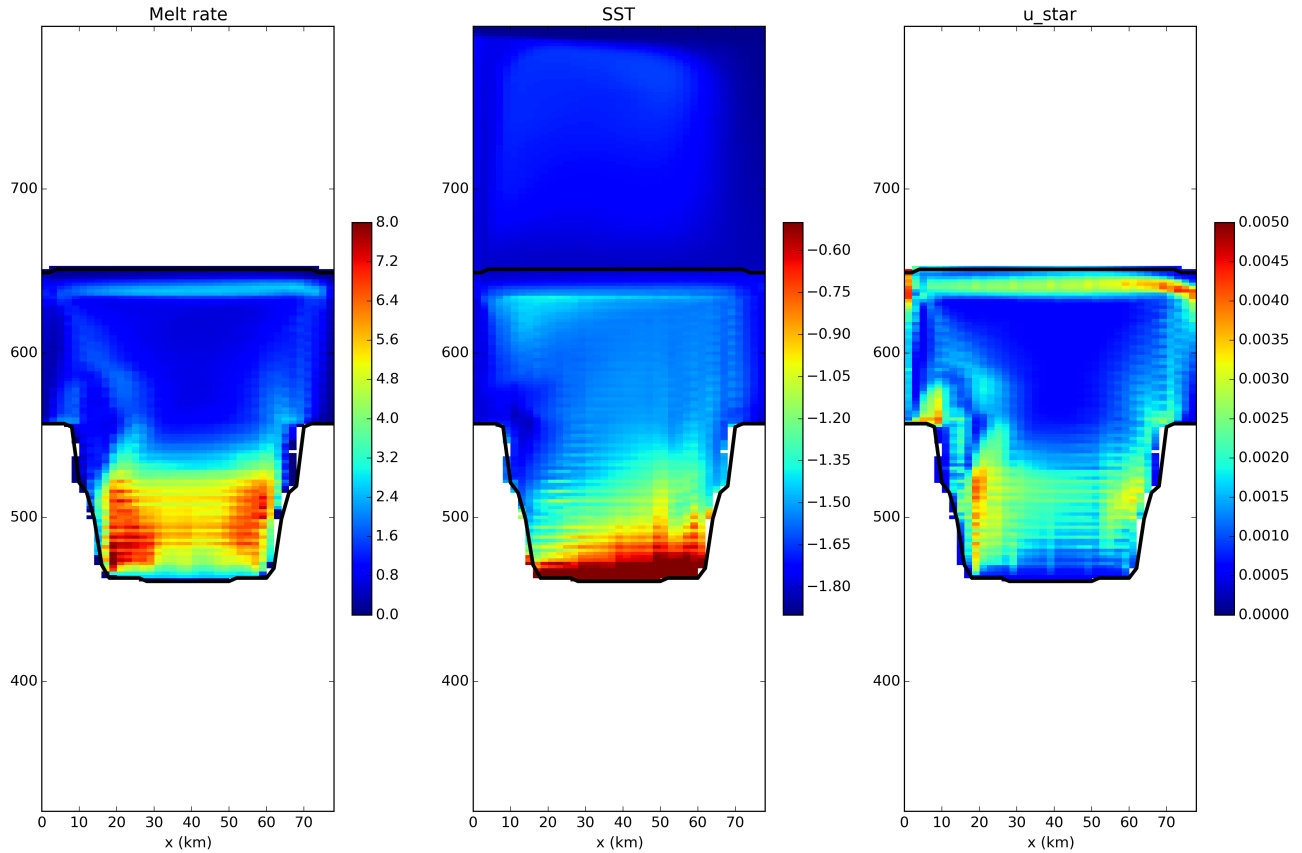


Figure S4. ALE Results of the static ice shelf experiment using the LIISM model. The three panels show 5 year time average of the (a) melt rate, (b) ocean surface temperature and (c) u^* in the top layer of the simulation (at the surface or directly below the ice shelf).

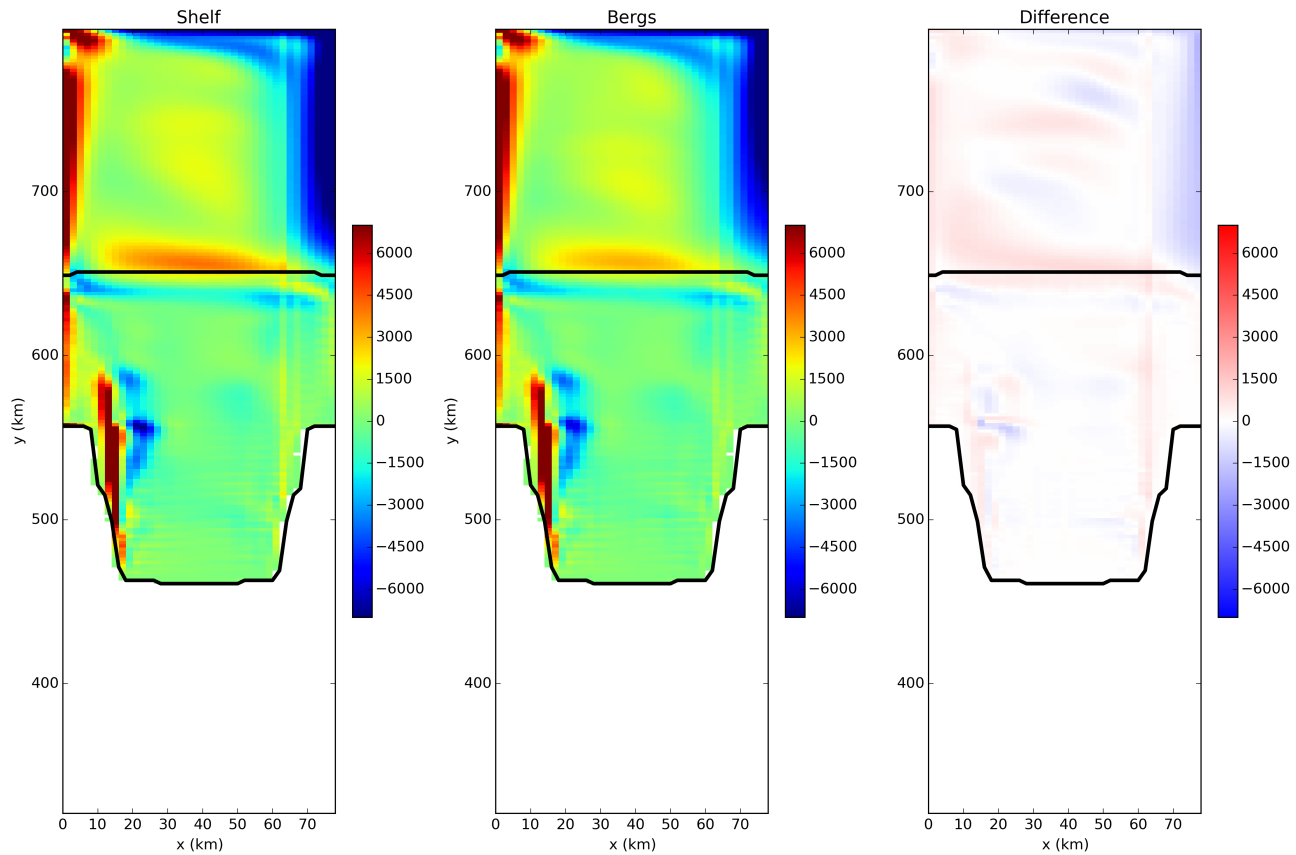


Figure S5. ALE Comparison of Eulerian ice shelf model and Lagrangian Ice shelf model barotropic stream function